Integrated Triassic sediment routing along eastern Gondwana (Australia)

Matthew Scipione[1], **Romain Vaucher**[1], **Eric Roberts**[2], **Alex J. McCoy-West**[1,5], **Joan Esterle**[3], **Ashten Turner**[1] **and Espen Knutsen**[1,4]

[1] *College of Science and Engineering , James Cook University, Townsville, Qld 4811, Australia*

[2]*Department of Geology and Geological Engineering, Colorado School of Mines, 1500 Illinois St, Golden, CO 80401, United States*

[3]*School of the Environment, The University of Queensland, Brisbane 4072, Australia*

[4]*Queensland Museum Tropics, Queensland Museum, Townsville, Queensland 4810, Australia*

[5]*Economic Geology Research Centre, James Cook University, Townsville, QLD, Australia*

Correspondence: Matthew Scipione (matt.scipione@my.jcu.edu.au)

ORCID number

Matthew Scipione: 0009-0000-7282-7419

Romain Vaucher: 0000-0003-3051-4128

Eric Roberts: 0000-0002-8583-7437

Alex McCoy-West: 0000-0003-4171-9276

Joan Esterle: 0000-0003-0775-5169

Espen Knutsen: 0000-0003-2646-2214

Keywords: detrital zircon, provenance, sediment routing, Bowen Basin, Triassic, Gondwana

Abstract

Triassic continental sedimentary basins along the eastern margin of Gondwana record drainage reorganisation and sediment routing, but provenance links among adjacent basins remain uncertain. This study integrates detrital zircon U–Pb data and sandstone petrography from the Triassic Rewan Group and Clematis Group of the northern Bowen Basin with published palaeocurrent constraints and compares these with published Triassic detrital zircon datasets from the Galilee Basin and the Gympie Terrane. Rewan Group zircon spectra are dominated by Middle Triassic grains (ca. 245 Ma) with persistent Carboniferous components. Sagittarius Sandstone and Arcadia Formation samples plot close together in a multidimensional scaling ordination of Wasserstein-2 distances, indicating similar age mixtures across the sampled Rewan Group depocentres. Short crystallisation-to-deposition age gaps and feldspar-poor, lithic-rich petrography are consistent with sustained volcaniclastic input from the eastern Tasmanide margin during Rewan Group deposition. Clematis Group spectra are more variable, contain fewer Triassic zircons, and include a larger proportion of grains older than ca. 400 Ma. More quartzose petrography and longer crystallisation-to-deposition age gaps suggest greater continental-interior input and/or increased recycling during later Triassic deposition. Regional comparisons place Rewan Group samples with the Bandanna Formation and Gympie Terrane units, whereas Clematis Group samples are closer to the Warang Sandstone and Porcupine Gorge Formation. Moolayember Formation reference spectra shift back towards a Rewan Group-like signal, suggesting that the Clematis Group provenance shift may have been temporally limited. These results provide a quantitative basis for testing basin connectivity and for linking changes in provenance to sediment routing within retroarc foreland systems.

Highlights

- Integrated provenance data help test sediment-routing change in retroarc basin systems.
- Rewan Group spectra record sustained sediment supply from an active continental margin.
- Clematis Group sandstones show increased inland and recycled sediment contributions.
- Regional comparisons identify source links among neighbouring eastern Australian basins.
- Results help explain how drainage networks reorganise in retroarc basin systems.

Introduction

Detrital zircon U–Pb geochronology is widely used to evaluate provenance and basin-scale sediment routing. Zircon is resilient to weathering and recycling, and age distributions can be compared quantitatively among stratigraphic levels and depositional systems (Adams et al., 2022; Andrade et al., 2023; Dickinson & Gehrels, 2009; Foley et al., 2021; Henderson & Fergusson, 2019; Li et al., 2015; Phillips et al., 2018; Romans et al., 2016; Rosenbaum et al., 2020; Shaanan et al., 2018; Shaanan & Rosenbaum, 2018; Sobczak et al., 2022; Todd, 2020; Tucker et al., 2013). In systems with multiple sediment sources, differences in zircon age spectra can result from shifts in source input, transport pathways, mixing, or recycling. To interpret these differences, datasets must be filtered consistently and compared using distribution-based similarity metrics. Detrital zircon data can also constrain maximum depositional ages when young grains are present, providing internal chronostratigraphic markers for correlation within and between depocentres (Foley et al., 2020, 2021; Tucker et al., 2016). This is particularly relevant to the Triassic of eastern Australia, when Late Permian–Triassic deformation reorganised drainage and altered sediment routing.

Eastern Australia includes retroarc basins adjacent to the Tasmanides, an accretionary orogenic belt along the eastern margin of Gondwana (Figure 1). Late Permian to Triassic shortening during the Hunter–Bowen Orogeny affected subsidence and relief across this system, which likely influenced drainage and sediment routing (Hoy, 2020; P.F. Li et al., 2012; Rosenbaum et al., 2020). The northern Bowen Basin (Figure 1) preserves Triassic fluvial to floodplain successions across multiple structural domains. It includes packages that can be used to test shifts between margin-derived detritus and cratonward or recycled sources. A key gap is that Triassic provenance links between the Bowen Basin, Galilee Basin, and Gympie Terrane remain uncertain (Figure 1). Existing detrital zircon datasets have uneven stratigraphic coverage and are often processed and reported using different conventions. This limits direct, quantitative comparison among basins and terranes. This study targets Triassic sandstones from the Rewan Group (Sagittarius Sandstone and Arcadia Formation) and the Clematis Group (Figure 2). These units span an interval in which sediment supply may have shifted from mainly margin-derived, arc-proximal sources to a more mixed signal with greater craton-derived and recycled input. Sandstone petrography and quartz–feldspar–lithic (QFL) point counts provide independent compositional context and help link zircon age populations to source lithologies and sediment dispersal pathways, but they do not uniquely resolve terrane-scale mixing, recycling, or basin-to-basin sediment transfer (Bashari, 2000; Grech, 2001; Kassan, 1994; Michaelsen & Henderson, 2000).

Published detrital zircon datasets provide useful regional reference points, but uneven coverage and differing workflows limit direct comparison. Gympie Terrane datasets provide an arc-proximal reference (Li et al., 2015; Rosenbaum et al., 2020), whereas Galilee Basin datasets provide a cratonward comparator and include signals of recycled basin fill (Phillips et al., 2018). Recycling and sediment transfer between basins can obscure source interpretations, so consistent methods and direct inter-basin comparison are required (Adams et al., 2022; Sobczak et al., 2022). These datasets define regional endmembers, but the northern Bowen Basin still lacks stratigraphically constrained, multi-proxy provenance data that can be directly compared with adjacent basins.

New stratigraphically constrained detrital zircon U–Pb data from Triassic sandstones in the northern Bowen Basin are integrated with sandstone petrography. Using the revised Rewan Group chronostratigraphy of Scipione et al. (2026), the analysis tests whether provenance shifts through the Rewan and Clematis groups reflect changes in source terranes, sediment-routing integration, or recycling.

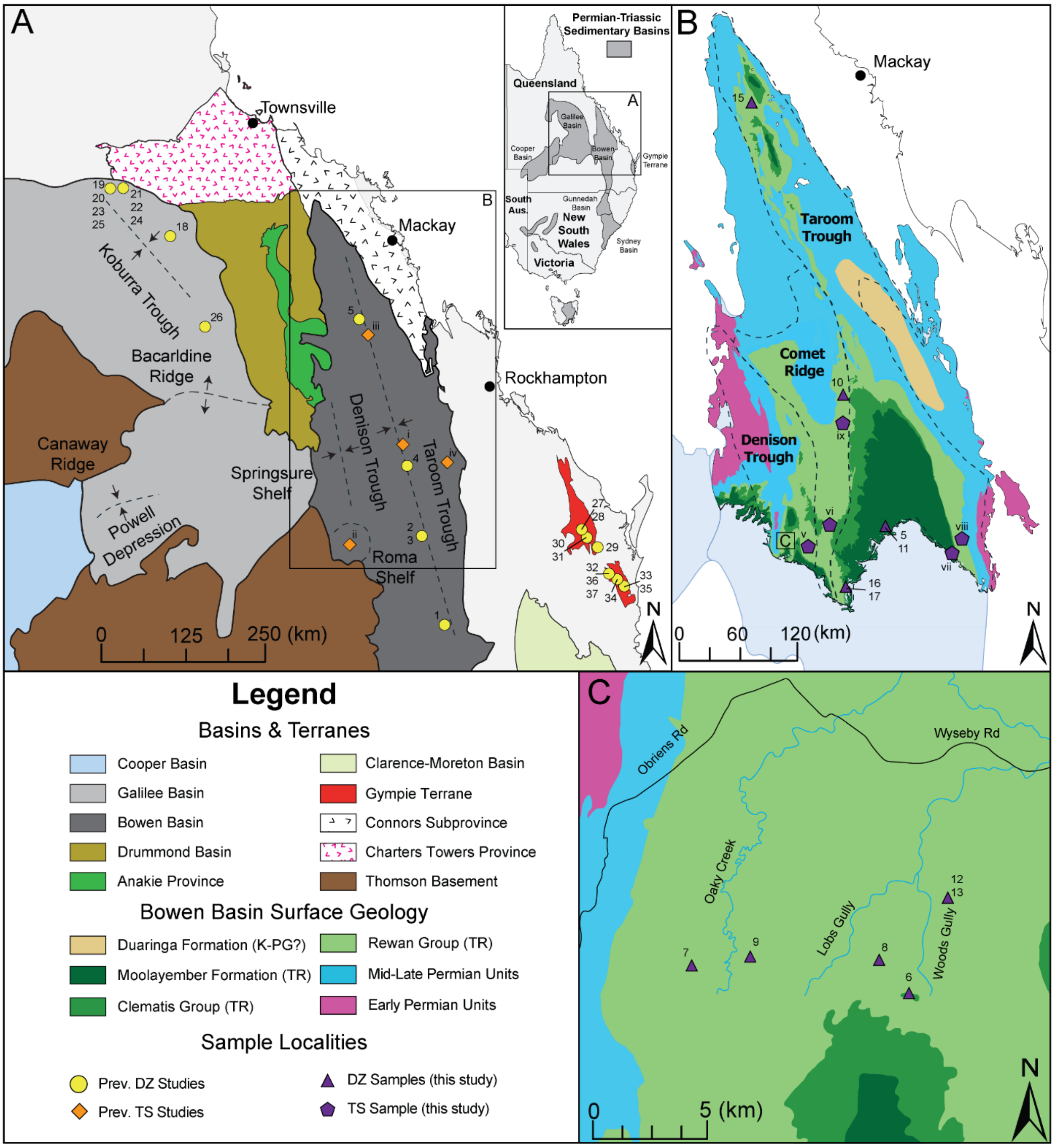

Figure 1. *(A) Regional map of Permian–Triassic basins and terranes in eastern Queensland, Australia, showing the locations of published detrital zircon (DZ) datasets compiled for regional comparison. Thin-section data are denoted by i = Kassan (1994), ii = Bashari (2000), iii = Michaelsen and Henderson (2000), and iv = Grech (2001). (B) Northern Bowen Basin map showing major structural elements (Taroom Trough, Denison Trough, and Comet Ridge) and the surface distribution of key stratigraphic packages. Symbols show sample localities for this study, including DZ samples and thin-section (TS) samples, together with locations from previous DZ and petrographic studies. Wells sampled for thin section in this study are denoted by v = Taroom 8, vi = Huntly 1, vii = Taroom 13, viii = Theodore NS150, and ix = Blackdown 3. (C) Enlarged inset of the Rewan area. Numbered labels adjacent to symbols identify individual sample localities and correspond to the sample numbering used in the Table 3. Symbols distinguish DZ and thin-section (TS) samples from this study and from previous studies.*

2. Geological background

2.1 Regional geology

The Bowen Basin lies within the Tasmanides of eastern Australia, an accretionary orogenic system that developed along the eastern Gondwanan margin through long-lived convergent-margin processes (Asmussen et al., 2023; Collins, 1991; Glen, 2005; Jessop et al., 2019; Rosenbaum et al., 2025). The Bowen–Gunnedah–Sydney Basin system extends from Townsville to Sydney (Figure 1). It records a transition from Early Permian extension to Late Permian–Triassic shortening and foreland-basin development during the Hunter–Bowen Orogeny and its post-orogenic adjustment (Brakel et al., 2009; Green et al., 1997; Jell, 2013; Korsch, Totterdell, Cathro, et al., 2009). During the Late Permian–Triassic interval, the deformation propagated into the basin and reorganised accommodation and relief, providing conditions for rapid changes in sediment routing, catchment, and recycling pathways (Babaahmadi et al., 2017; Campbell et al., 2017; Hoy, 2020; Hoy et al., 2018). The study area in the northern Bowen Basin, Queensland, lies close to the coastal part of the orogen and along potential pathways for craton-derived sediment (Figure 1A), providing a strong position to evaluate competing provenance models using stratigraphically constrained detrital zircon (DZ) data.

From a provenance perspective, the main potential sediment sources are the New England Orogen (NEO) and related arc terranes near the former plate margin, and the more inland Thomson Orogen and associated basement provinces that underlie and border the foreland basin (Baker, 1997; Glen, 2005; Jessop et al., 2019; Sobczak et al., 2022). The NEO is a composite system of accreted terranes and magmatic belts and is commonly treated as the main eastern sediment source for Permian–Triassic basins in Queensland (Collins, 1991; P.F. Li et al., 2012; Rosenbaum et al., 2025; Siegel et al., 2020). Continued convergence, rollback, and arc reconfiguration into the Triassic provide a mechanism for sustained delivery of near-contemporaneous zircon to adjacent depocentres, either by direct erosion of arc and plutonic sources or by recycling of volcaniclastic successions (Campbell et al., 2022; Jessop et al., 2019; Li et al., 2015; Rosenbaum, 2026; Sliwa et al., 2018). If the NEO dominated sediment supply, Triassic DZ spectra would be expected to be rich in Late Palaeozoic–Triassic ages, with secondary Devonian–Carboniferous and older Palaeozoic components derived either from Tasmanide basement or recycled basin fill (Foley et al., 2021; Todd et al., 2022; Tucker et al., 2016).

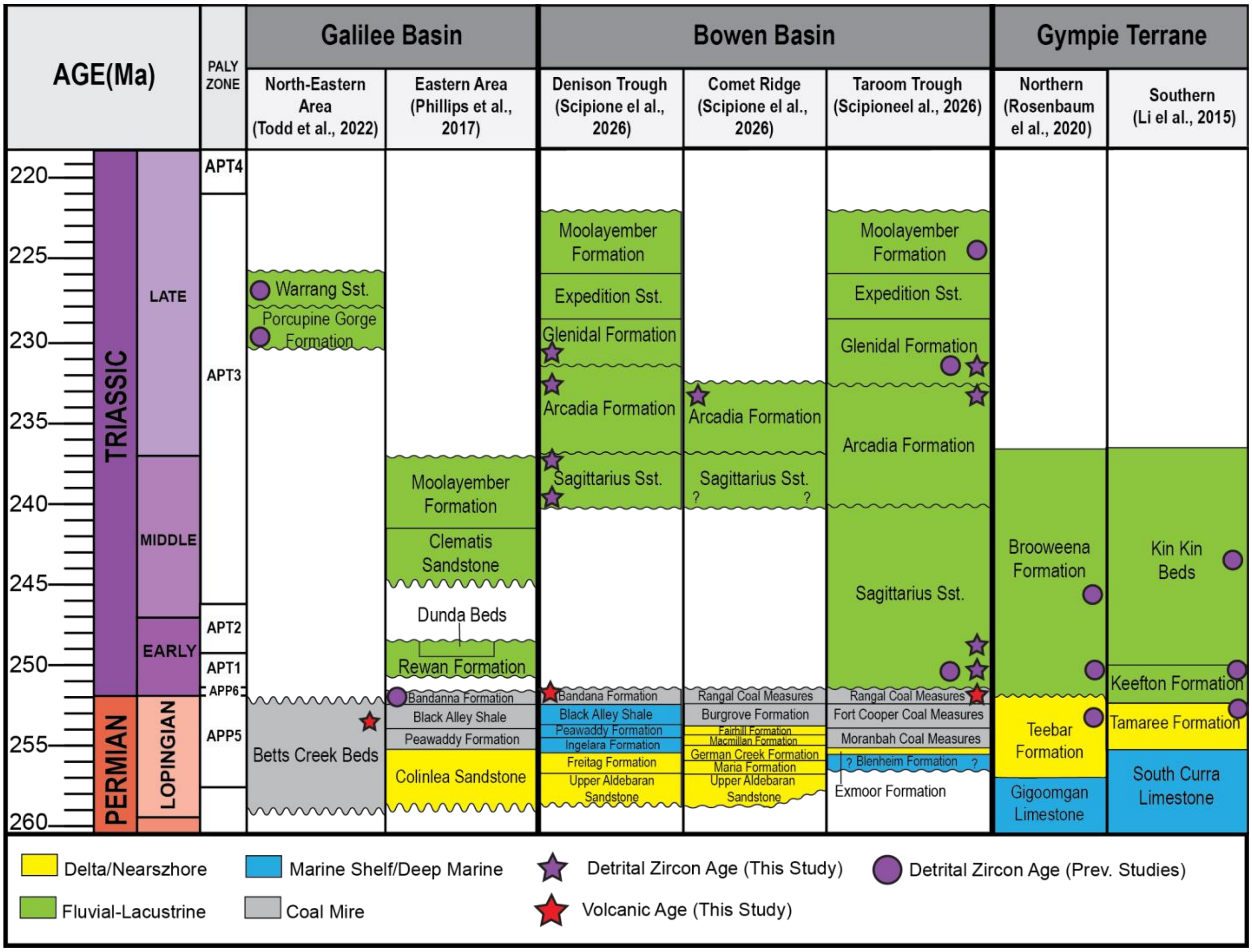

Figure 2. Composite stratigraphic columns show major lithostratigraphic units plotted against age and palynological zonation, with broad depositional environments indicated by colour. Symbols mark detrital zircon (DZ) maximum depositional ages from this study and previously published DZ ages from the Galilee Basin and Gympie Terrane datasets used for regional comparison.

The Thomson Orogen underlies the Bowen–Galilee region and is locally exposed in basement inliers such as the Anakie Inlier and Charters Towers Province (Figure 1A; Jell, 2013). Thomson-related DZ spectra commonly include Neoproterozoic–Cambrian and Mesoproterozoic Grenvillian populations, although these overlap with other Tasmanide sources (Asmussen, 2020; Purdy et al., 2016; Sobczak et al., 2022; Spampinato et al., 2015). These cratonward modes could enter Triassic foreland strata through western catchments, recycling of older sedimentary rocks, or along-basin transport between depocentres (Korsch, Totterdell, Fomin, et al., 2009; Sobczak et al., 2022).

The Galilee Basin (Figure 1A) provides the main cratonward comparison because it lies adjacent to the Bowen Basin and overlies Thomson Orogen crustal domains that could have supplied sediment from the west or northwest to Triassic successions (Phillips et al., 2018; Todd, 2020; Todd et al., 2022; Van Heeswijck, 2010, 2018). Published DZ datasets from the basin record mixed age populations that include both cratonward basement signatures and Tasmanide margin components and thus provide a practical regional comparator (Phillips et al., 2018; Todd et al., 2022). At the active-margin side of the foreland system, the Gympie Terrane provides the arc-proximal benchmark for Triassic detrital zircon age populations (Li et al., 2015; Rosenbaum et al., 2020).

2.2 Bowen Basin framework and stratigraphy

The Triassic succession of the northern Bowen Basin is underlain by the upper Permian Blackwater Group, which forms the underlying unit and an important reference for provenance analysis (Figure 2). Within the Blackwater Group, the Bandanna Formation and related coal measures comprise alternating marine mudstones, coal-rich intervals, and fluvial sandstones that record repeated shifts in accommodation and shoreline position during late Permian foreland basin fill (Fielding et al., 2022; Naher et al., 2025; Phillips et al., 2017, 2018). These upper Permian units are relevant to Triassic provenance because they include regionally traceable volcanic ash beds that provide age anchors close to the Permian–Triassic transition (Ayaz et al., 2016; Brakel et al., 2009; Grech, 2001; Green et al., 1997; Korsch, Totterdell, Fomin, et al., 2009; McKellar et al., 2015; Scipione et al., 2026).

Continental red-bed deposition of the Rewan Group marks a major shift in depositional style following the cessation of coal accumulation and the associated wetland environments in the latest Permian succession (Fielding et al., 1997; Grech, 2001; Jensen, 1975; Lang et al., 2001). The basal Triassic surface is commonly expressed as an erosional contact, but the stratigraphic expression and duration of missing section vary across structural domains (Exon, 1976; Grech, 2001; Green et al., 1997). New chronostratigraphic constraints indicate that the contact is time transgressive and that preservation differs between the foredeep and the backbulge at the scale of the northern basin (Scipione et al., 2026). In the Taroom Trough foredeep, depositional ages and maximum depositional ages from the lowermost Triassic red beds show progressive younging above the latest Permian deposits, consistent with relatively continuous accommodation and sedimentation through the Early and Middle Triassic at the resolution of the detrital record (Scipione et al., 2026). In contrast, the Denison Trough (backbulge) preserves a condensed Triassic record above the latest Permian horizons, suggesting a substantial interval of non-deposition and/or erosion across the Permian-Triassic transition (Scipione et al., 2026). This spatial contrast is central to the provenance framework because it influences both the completeness of the stratigraphic archive and the likelihood that older successions were exposed for recycling during early Triassic basin evolution.

The Sagittarius Sandstone forms the basal fluvial package of the Rewan Group and records the earliest preserved phase of continental drainage development within the Triassic succession (Figure 2). It is typically composed of fine- to medium-grained channel sandstones with trough cross-bedding, ripple lamination, and scour surfaces, interbedded with thick red siltstone and mudstone floodplain deposits (Exon, 1976; Grech, 2001; Green et al., 1997; Jensen, 1975; Lang et al., 2001). The basal surface of the Sagittarius Sandstone is commonly treated as a sequence boundary associated with regional base-level fall and incision at the Permian–Triassic transition, but its expression varies between structural domains and may be time transgressive at the scale of the northern basin (Brakel et al., 2009; Grech, 2001; Scipione et al., 2026). The overlying Arcadia Formation comprises a several hundred metres thick succession of fluvial channel and overbank deposits that grades upward into mud-rich floodplain intervals with palaeosols and pedogenic carbonate, consistent with prolonged floodplain aggradation under arid to semiarid conditions (Brakel et al., 2009; Exon, 1976; Grech, 2001; Jensen, 1975; Lang et al., 2001). Within the Arcadia Formation, coarse-grained sandstone bodies such as the Brumby Sandstone Member have been interpreted as channelised packages that record changes in accommodation and sediment supply within broader Rewan Group evolution (Grech, 2001; Lang et al., 2001). Rewan Group sandstones are also characterised by abundant volcaniclastic detritus, consistent with strong sediment supply from the NEO and contemporaneous magmatic activity along the active margin (Bashari, 2000; Michaelsen & Henderson, 2000).

A further basin-scale change occurs at the base of the Clematis Group, where quartz-rich, commonly pebbly sandstones rest sharply on Rewan Group red beds in many parts of the basin (Brakel et al., 2009; Jensen, 1975; Kassan, 1994). Clematis Group deposits are more texturally and compositionally mature than the underlying Rewan Group and have been linked to changing sediment supply and drainage during waning Hunter–Bowen deformation, although longer transport, storage, and recycling may also have amplified the signal (Baker, 1997; Brakel et al., 2009; Grech, 2001; Kassan, 1994; Korsch, Totterdell, Fomin, et al., 2009; Michaelsen & Henderson, 2000). The Moolayember Formation caps the Triassic succession and includes a laterally persistent basal flooding interval, but the extent and mechanism of any marine influence remain uncertain (Brakel et al., 2009; Grech, 2001; Green et al., 1997). Together, the Bandanna Formation and overlying Triassic units provide the framework for testing whether provenance signals track margin-derived volcaniclastic supply during Rewan Group deposition and whether more mature, cratonward-derived sediment became more important during Clematis Group and younger Triassic deposition (Figure 2).

2.3 Previous detrital zircon U-Pb geochronology

Regional detrital zircon U–Pb datasets provide the basis for comparing Triassic sediment routing among eastern Australian basins. Gympie Terrane datasets provide an arc-proximal reference, Galilee Basin datasets provide a cratonward reference, and Bowen Basin system datasets provide broader context for provenance mixing and sediment redistribution (Adams et al., 2022; Li et al., 2015; Phillips et al., 2018; Sobczak et al., 2022; Todd et al., 2022). The geographic and stratigraphic relationships of these datasets are summarised in Figures 1 and 2.

Detrital zircon spectra are not unique fingerprints, so zircon ages are interpreted alongside independent provenance and transport constraints. Recent studies have expanded regional DZ coverage and improved stratigraphic frameworks in adjacent basins, but a Triassic provenance synthesis for the northern Bowen Basin is still lacking (Adams et al., 2022; Sobczak et al., 2022). The regional comparison is used to identify broad provenance patterns rather than exact sample-to-sample equivalence, because sampling density, analytical workflow, and stratigraphic correlation vary among studies (Andrade et al., 2023; Li et al., 2015; Phillips et al., 2018; Todd et al., 2022).

Accordingly, published Triassic datasets from the Galilee Basin and Gympie Terrane (Adams et al., 2022; Li et al., 2015; Phillips et al., 2018; Rosenbaum et al., 2020; Sobczak et al., 2022; Todd et al., 2022) are compiled, reprocessed using a single filtering and reporting workflow, and compared directly with new stratigraphically constrained Triassic detrital zircon data from the northern Bowen Basin. This framework tests whether provenance patterns reflect persistent arc-dominated supply, increased continental interior contribution, or recycling driven mixing. It also tests whether basin-to-basin similarities reflect shared source access rather than coincidence.

3. Methods

3.1 Sampling strategy and sample context

Detrital zircon samples were collected from outcrop and archived drill core across the northern Bowen Basin, Queensland (Figure 1B, C). Petrographic sampling focused on core intervals where continuous stratigraphic control is available. Surface exposures were combined with subsurface control from multiple wells to capture provenance variability along strike and across structural domains. Archived drill core was accessed through the Geological Survey of Queensland core library in Brisbane. Sampling targeted biotite-rich sandstone to maximise zircon recovery and improve recovery of the youngest detrital component for MDA estimation. Typical outcrop sample mass was 1–5 kg, and core samples were taken over half-core intervals of approximately 15 cm.

The DZ dataset includes outcrop samples from the Arcadia Formation and basal Clematis Group. Arcadia Formation sandstones were sampled at Early Storms Creek, The Crater, Oaky Creek (Early Storms Station), and Duckworth Creek (Figure 1B, C). A Clematis Group sandstone was collected at Mount Round (Figure 1C) to provide an upper stratigraphic comparison to the Rewan Group interval. Core-based DZ sampling provides stratigraphic control through key intervals and extends coverage across depocentres in the northern Bowen

Basin (Figure 1B). Core samples were collected from Rewan 1, Brumby Plains 1, Taroom 14, Drake NS27, and Theodore NS150 (Figure 1B, C).

Petrographic thin sections were prepared from a targeted subset of samples to provide compositional context for the DZ-based provenance interpretation and to support QFL classification. Representative photomicrographs include Bandanna Formation, Sagittarius Sandstone, Arcadia Formation, and Clematis Group samples from Taroom 8, Drake NS27, Blackdown 3, Huntly 1, Theodore NS150, Taroom 14, and Taroom 13. These include both DZ-analysed intervals and additional intervals used to broaden petrographic coverage.

3.2 Sandstone Petrography

Sandstone petrography was undertaken on 35 thin sections prepared from core samples across the northern Bowen Basin study area (Figure 1). The thin sections span the Bandanna Formation, Sagittarius Sandstone, Arcadia Formation, and Clematis Group (Figures 2, 3; Table 1). Selected photomicrographs are presented in Figures 4 and 5 to illustrate key grain types, textures, and diagenetic features observed within each stratigraphic package.

Framework composition was quantified using QFL (quartz, feldspar, lithic fragments) point counting following the Gazzi-Dickinson approach (Dickinson & Suczek, 1979; Ingersoll et al., 1984). Each thin section was point counted on a systematic grid, with a target of ~300 points per section. Framework grains, matrix, and pore space/diagenetic components were recorded separately to allow reproducible comparison among stratigraphic units. Counts were assigned to quartz, feldspar, lithic fragments, and matrix. Porosity, accessory minerals, authigenic minerals, and cements were excluded from the framework tally. Matrix was recorded during point counting but excluded from the QFL framework normalisation, so that plotted compositions represent only QFL (Figure 3).

Sandstone compositions were interpreted using the QFL classification of Garzanti (2016, 2019) and the provenance fields of Dickinson and Suczek (1979) and Dickinson et al. (1983). These plots are used to provide first order constraints on sediment character and source type and to complement detrital zircon provenance interpretations, rather than as a unique indicator of tectonic setting (Figures 4, 5).

3.3 Detrital zircon U–Pb geochronology

Samples were crushed and milled, and the <500 μm fraction was retained for mineral separation. Heavy mineral concentrates were produced using standard density and hydraulic methods, including Wilfley table concentration followed by heavy liquid separation (LMT; density 2.87). Zircons were handpicked under a binocular microscope. Approximately 300 grains per sandstone sample were mounted in epoxy, polished to expose grain midsections, and carbon coated. Zircons were imaged by a Hitachi SU5000 scanning electron microscope with a cathodoluminescence filter (SEM-CL) to document internal zoning and to guide placement of ablation pits away from cracks, inclusions, and mixed domains.

U–Pb analyses were conducted at the Advanced Analytical Centre (AAC), James Cook University (JCU), Townsville, Australia, using a 193 nm ArF excimer laser coupled to an Agilent 8900 ICP–MS. Analyses used a 20 μm spot diameter at 10 Hz, with fluence maintained at 5–10 J/cm². Each analysis comprised a gas blank followed by 30–45 s of ablation. Primary and secondary zircon reference materials (GJ-1 and Temora-2) were analysed throughout each session to calibrate and monitor accuracy, bracketing groups of unknowns, and NIST 610 glass was used to monitor instrument behaviour and stability through time.

Data reduction was completed using Iolite/VizualAge following standard workflows for background subtraction, downhole fractionation correction, and drift correction (Paton et al., 2011). Analyses were screened for unstable signals and mixed-domain behaviour.

Uncertainties are reported at 2σ and include propagated external uncertainties based on session standards. Discordance was assessed using $^{206}Pb/^{238}U$ and $^{207}Pb/^{235}U$ systematics. Unless stated otherwise, detrital zircon analyses with >10% discordance were excluded from age spectra, Wasserstein-2 dissimilarity calculations, and maximum depositional age estimates. For grains younger than *ca.* 1500 Ma, $^{206}Pb/^{238}U$ ages were used; for older grains, $^{207}Pb/^{206}Pb$ ages were used.

3.4 Statistical and graphical workflow

Age spectra were visualised using kernel density estimates (KDEs) and cumulative distribution functions (CDFs). KDEs were used to show multimodal structure without binning artefacts, whereas CDFs were used for quantitative comparisons because they preserve the empirical rank structure of the data (Vermeesch, 2012). KDE shape depends on bandwidth and kernel choice, so KDEs are used here only as a qualitative visual aid. Quantitative comparisons are based on CDF-derived statistics from the filtered dataset. For the formation-level composites shown in Figure 6, concordant analyses were also grouped into broad regional age-population bins to calculate the percentage contribution of each interval (Table 2). These percentages are used as summary descriptors of relative age-population abundance and do not replace the distribution-based comparisons (Figure 6, 7, 8).

Between-sample similarity was assessed using distance-based methods and ordination. Pairwise dissimilarity was quantified using the Wasserstein-2 distance calculated from empirical CDF, and the results were visualised using multidimensional scaling (MDS) (Vermeesch, 2018; Lipp & Vermeesch, 2022). The Wasserstein-2 distance measures the amount of distributional shift required to transform one age distribution into another. MDS projects the resulting pairwise distance matrix into two dimensions. Samples that plot close together therefore have similar overall age distributions, whereas samples that plot farther apart are more dissimilar. Dim 1 and Dim 2 are unitless ordination axes. No direct geological meaning is assigned to the axes themselves. Instead, the ordination is interpreted by comparison with the KDEs and other provenance constraints. To evaluate source-to-sink implications through time, crystallisation-to-deposition age-gap plots were used to compare zircon crystallisation ages with depositional constraints (Cawood et al., 2012). These plots are used here as interpretive context for provenance, not as stand-alone tectonic discriminants (Figure 7).

Maximum depositional ages (MDA) were calculated to provide internal depositional constraints for stratigraphic comparison and for lag-time calculations. MDA were estimated using multiple approaches that capture different assumptions about the youngest population: (i) the youngest single grain (YSG), (ii) the youngest grain cluster (YGC), and (iii) a maximum likelihood age (MLA) estimate (Table 3; Vermeesch, 2021). MDA were calculated from <10% discordant analyses and were only treated as meaningful where the youngest population forms a coherent cluster of overlapping ages and where results are consistent with stratigraphic order (Coutts et al., 2019; Dickinson & Gehrels, 2009).

3.5 Compilation and standardisation of published detrital zircon datasets

Published detrital zircon datasets from surrounding basins and terranes were compiled from supplementary material to place the northern Bowen Basin results in a regional framework. The compiled datasets include Triassic and closely adjacent successions from the Galilee Basin (Phillips et al., 2018; Todd, 2020; Todd et al., 2022), the Gympie Terrane (Li et al., 2015; Rosenbaum et al., 2020) (Figure 1A), and the Surat Basin, including Triassic Moolayember Formation samples used for comparison (Figure 9) (Sobczak et al., 2022). Additional Triassic samples from adjacent basins and terranes were taken from the regional compilation of Adams et al. (2022).

Only studies that provide grain-scale ages (or equivalent downloadable tables) were included. Where raw ages and uncertainties were available, datasets were re-filtered using a consistent <10% discordance threshold and the same age-selection rules applied to the new data. Where only pre-filtered concordant datasets were published, the original filtering criteria were retained and documented (Table 3). Published comparison datasets therefore vary in concordant grain count and, in some cases, in original analytical and filtering workflow. Accordingly, the regional comparison emphasises broad and reproducible similarity structure rather than exact equivalence among all published spectra.

3.6 Palaeocurrent

Palaeocurrent data used in this study were compiled from published measurements rather than collected as part of this work. The compiled dataset includes palaeocurrent indicators reported for Triassic strata in the northern Bowen Basin and is used to provide independent constraints on sediment transport directions for the palaeodrainage reconstructions and routing interpretations. Palaeocurrent vectors shown in Figure 10 are taken from Jensen (1975), Kassan (1994), and Grech (2001). Palaeocurrent measurements are plotted as reported in the original sources; where the original studies indicate structural (tilt) correction, their corrected orientations are retained, and where correction status is unclear, the vectors are treated as qualitative indicators of transport direction rather than definitive directional information.

4. Results

4.1 Petrography and QFL compilation results relevant to provenance

Petrographic results are summarised using QFL ternary plots and Dickinson-style provenance fields (Figure 3) with representative thin-section images (Figures 4 and 5). Across units, most point-count data plot near the quartz–lithic join, indicating low feldspar contents (Figure 3).

Blackwater Group samples plot towards the lithic-rich side of QFL space and cluster near the quartz–lithic join (Figure 3A). In the provenance discrimination plot, they fall mainly within transitional to lithic recycled fields (Figure 3B). The Bandanna Formation thin section shows abundant lithic grains and calcite cement (Figure 4A).

Rewan Group samples show broader dispersion along the quartz–lithic axis and plot closer to the lithic corner than Clematis Group samples (Figure 3C). In the Dickinson diagram, Rewan Group samples plot mainly in transitional recycled and magmatic-arc fields (Figure 3D). Thin sections from the Sagittarius Sandstone contain volcanic rock fragments and feldspar, and carbonate cement is locally present (Figure 4B–D). Arcadia Formation thin sections show the same framework components, with zircon as an accessory phase and local carbonate cement (Figure 5A–B). The new Rewan Group point counts overlap the compiled datasets plotted in Figure 3 and extend coverage for samples from the Taroom Trough.

Clematis Group samples plot towards the quartz-rich side of the QFL diagram and fall mainly within quartzose recycled to transitional recycled fields (Figure 3E–F). Thin sections from the Clematis Group show quartz-rich frameworks with subordinate feldspar and variable lithic fragments (Figure 5C–D).

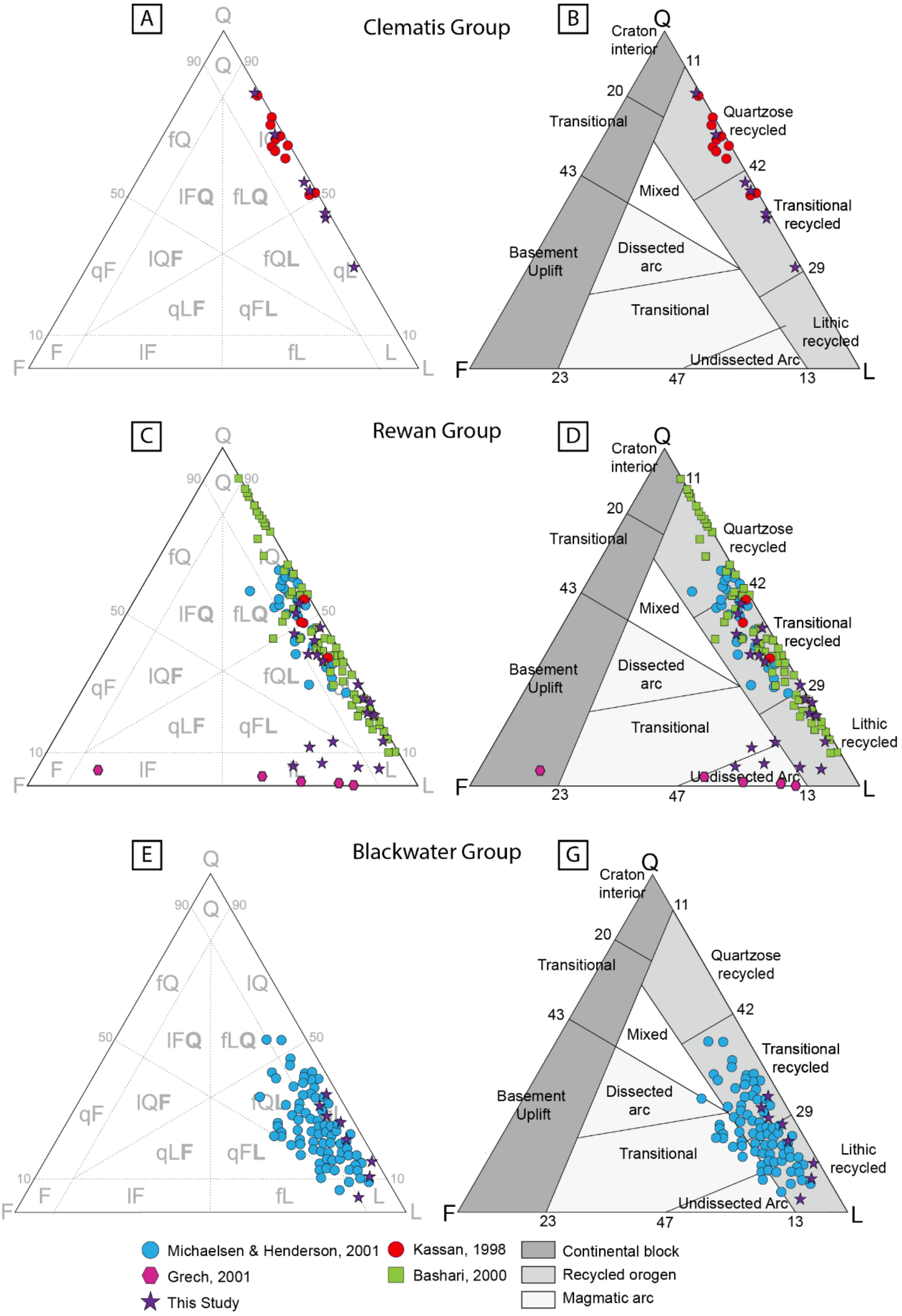

Figure 3. *Quartz–feldspar–lithic classification diagrams (A, C, E) use the sandstone classification of Garzanti (2016, 2019). Provenance discrimination diagrams (B, D, F) follow Dickinson and Suczek (1979) and Dickinson et al. (1983) and show continental block, recycled orogen, and magmatic arc fields. Panels A–B show Blackwater Group samples, panels C–D show Rewan Group samples, and panels E–F show Clematis Group samples. Data compiled from Kassan (1994), Bashari (2000), Michaelsen & Henderson (2000), and Grech (2001) are plotted alongside new point-count data from this study.*

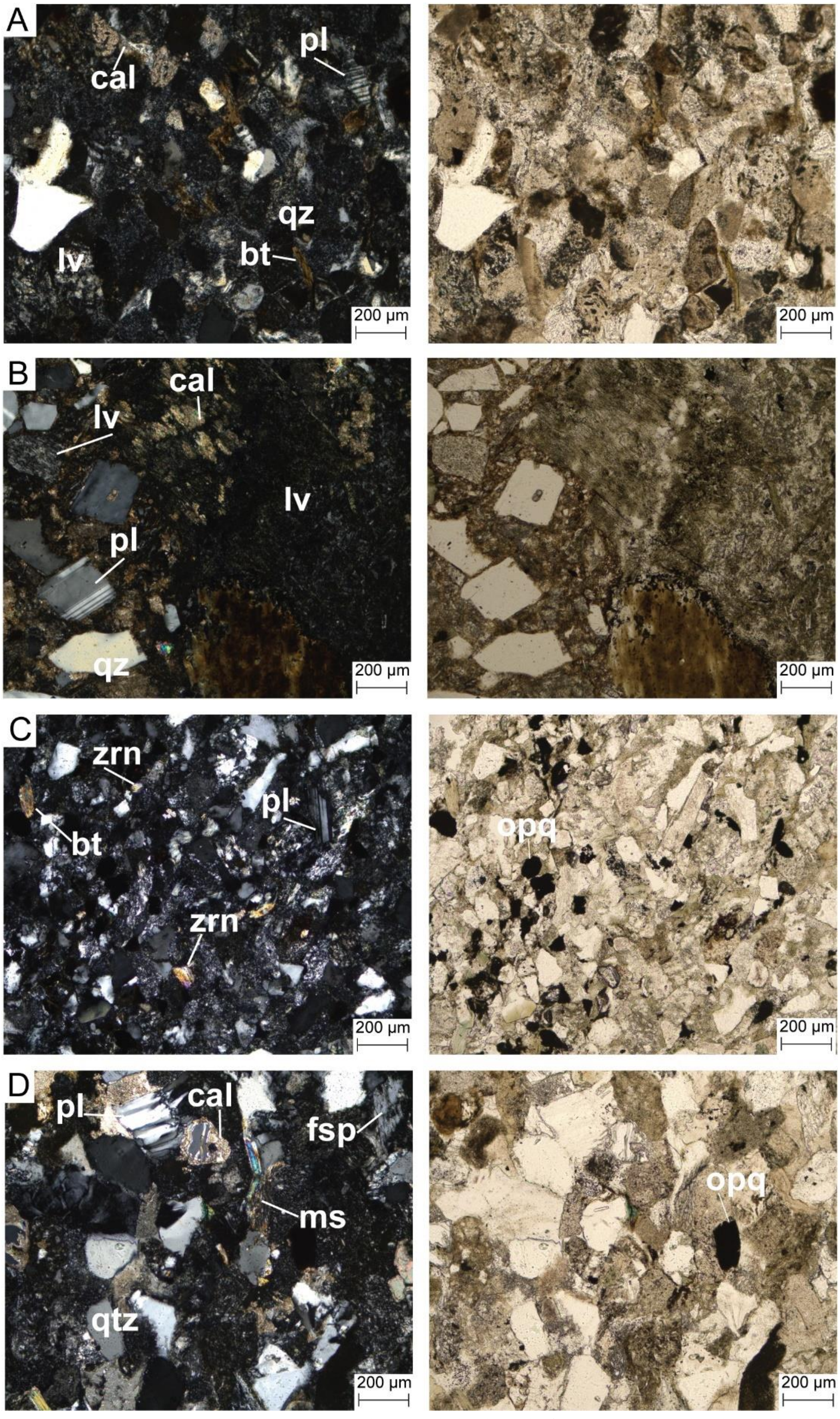

Figure 4. *Paired images show cross-polarised light (left; XPL) and plane-polarised light (right; PPL) views for each sample. (A) Taroom 8, 552 m (Bandanna Formation). (B) Theodore NS150, 171 m (Sagittarius Sandstone). (C) Drake NS 27, 131 m (Sagittarius Sandstone). (D) Taroom 8, 408 m (Sagittarius Sandstone). Mineral abbreviations:* ***bt*** *= biotite;* ***cal*** *= calcite;* ***opq*** *= Fe-oxide/opaque grain;* ***fsp*** *= feldspar;* ***ms*** *= muscovite;* ***pl*** *= plagioclase;* ***qz*** *= quartz;* ***lv*** *= volcanic rock fragment;* ***zrn*** *= zircon.*

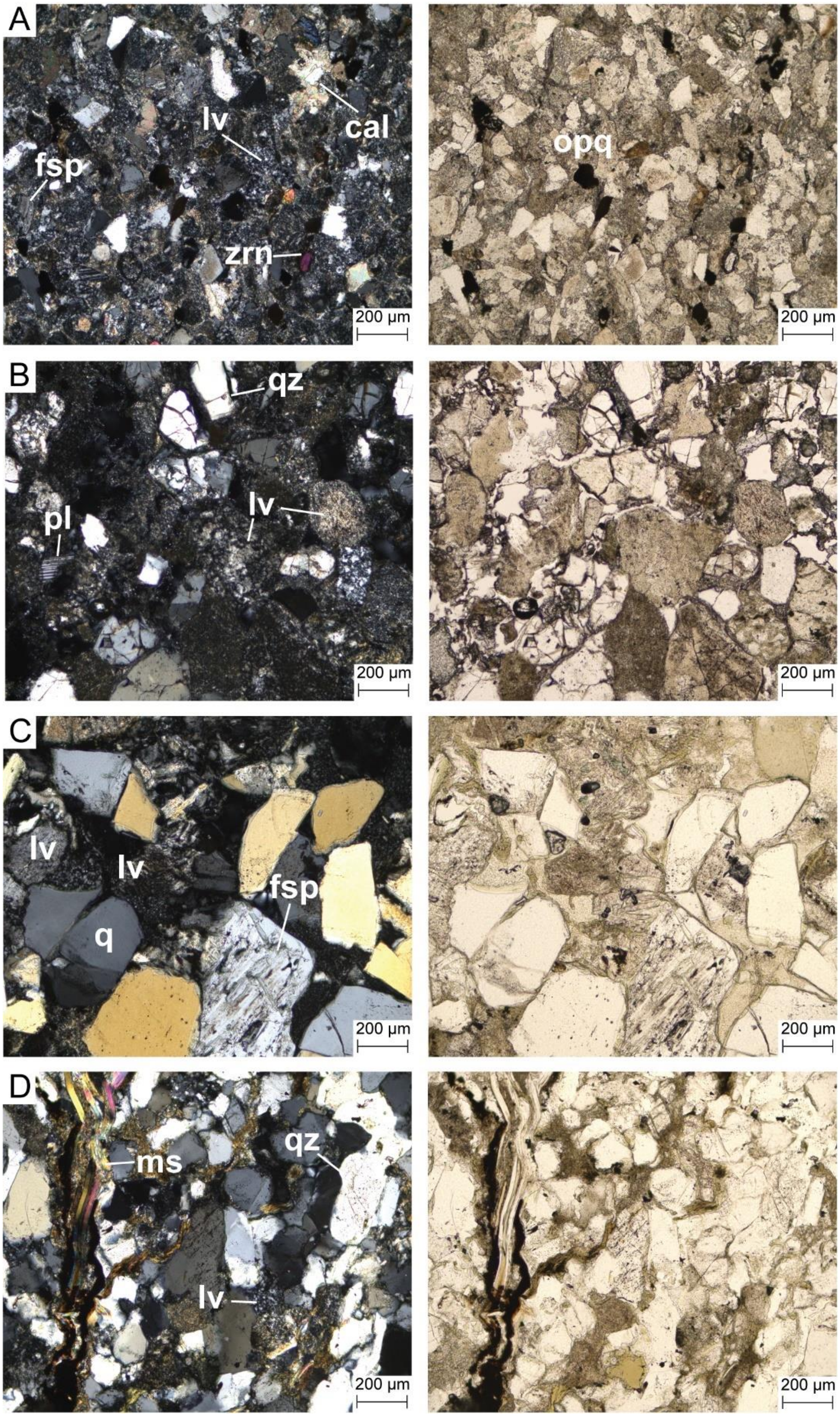

Figure 5. *Paired images show cross-polarised light (left; XPL) and plane-polarised light (right; PPL) views for each sample. (A) Taroom 14, 1144 m (Arcadia Formation). (B) Taroom 8, 217 m (Arcadia Formation). (C) Taroom 13, 765 m (Clematis Group). (D) Taroom 14, 904 m (Clematis Group). Mineral abbreviations:* ***bt*** *= biotite;* ***cal*** *= calcite;* ***opq*** *= Fe-oxide/opaque grain;* ***fsp*** *= feldspar;* ***ms*** *= muscovite;* ***pl*** *= plagioclase;* ***qz*** *= quartz;* ***lv*** *= volcanic rock fragment;* ***zrn*** *= zircon.*

Table 1. *Petrographic characteristics of sandstone samples summarised for each stratigraphic interval. Q – quartz, F – feldspar, L – lithic fragments*

Stratigraphic interval (unit) (n=number of samples)	QFL %	Quartz properties	Grain size	Cements, porosity and matrix	Textural maturity	Lithic grains	Accessory minerals	Ref. figure(s)
Blackwater Group (n=7)	Q: 10.4–34.6% F: 1.2–6.3% L: 62.3–85.7%	Both mono- and polycrystalline varieties present	Fine to medium grained sand	Calcite cement occurs in this study's Bandanna panel.	Low to moderate	Volcanic lithic fragments dominate	Biotite present; minor opaques and zircons.	Fig. 4A
Sagittarius Sandstone (tuffaceous debris flow; GSQ Theodore NS150) (n=2)	Q 5.7–6.4% F 21.3–29.1% L 65.2–72.3%	minor mono- and polycrystalline varieties	Fine grained to pebbles	Carbonate occurs as cement and as an alteration product; chlorite alteration is strong	Immature (angular, poorly sorted; limited reworking)	Dominated by igneous rock fragments, including abundant trachyte; basaltic fragments noted; plagioclase is euhedral and twinned (volcanic origin)	Zircon and mica occur as accessory phase; minor pyrite	Fig. 4B
Sagittarius Sandstone (fluvial sandstones) (n=12)	Q 4.7–50.9% F 0.6–22.2% L 43.4–87.8%	Monocrystalline quartz dominates and minor polycrystalline varieties present	Fine to medium grained sand	Calcite pore-filling cement and early siderite occur in Rewan lithic sandstones regionally	Low to moderate	Volcanic lithics dominate many intervals	Authigenic phases in Rewan lithic sandstones include calcite, siderite, chlorite, kaolin/illite (context for cement/matrix expectations)	Fig. 4 C-D
Arcadia Formation (n=6)	Q: 20.6–53.9% F: 0.0–8.6% L: 42.5–78.5%	Monocrystalline quartz dominates and minor polycrystalline varieties present	Fine to medium grained sand	Calcite is a common pore-filling cement; siderite and quartz overgrowths may occur	Low to moderate; typically, subangular grains	Volcanic lithic fragments dominate and sporadic chert	Muscovite, zircon present, feldspar (incl. plagioclase)	Fig. 5 A-B
Clematis Group (n=7)	Q: 30.1–81.4% F: 1.2–2.6% L: 17.0–68.4%	Monocrystalline quartz dominates	Fine to very coarse-grained sand	Patchy cement and variable matrix; porosity varies between samples.	Low to moderate	Mostly sparse lithics in quartzose intervals; where present, volcanic fragments occur (this study).	Muscovite common in Clematis; zircon present as an accessory phase.	Fig. 5 C-D

4.2 Detrital zircon age spectra

Detrital zircon U–Pb results are presented for 12 sandstone samples from the Rewan Group and Clematis Group. Sample locations are shown in Figure 1 and the stratigraphic grouping is summarised in Figure 2. Age spectra are shown as formation-level composites (Figure 6) and for the full dataset (Figure 7A). Samples from the same stratigraphic unit were combined to summarise unit-scale detrital signatures, and concordant analyses were also grouped into broad age-population bins for percentage comparison (Table 2).

The filtered Bowen Basin dataset includes 2212 grains. These are partitioned into 927 grains from the Sagittarius Sandstone, 871 grains from the Arcadia Formation, 183 grains from the Clematis Group in the Denison Trough, and 231 grains from the Clematis Group in the Taroom Trough (Figure 6). The combined spectrum is dominated by Phanerozoic ages, with the highest densities between ca. 200 and 450 Ma and subordinate older Palaeozoic and Proterozoic components (Figure 7A). Modes in the full dataset occur near ca. 245 Ma, ca. 312 Ma, and ca. 341 Ma (Figure 7A).

The Sagittarius Sandstone is characterised by a dominant Triassic mode near *ca*. 246 Ma and secondary modes near *ca*. 303 Ma and *ca*. 353 Ma (Figure 6D). The overlying Arcadia Formation shows a dominant Triassic mode near *ca*. 245 Ma with secondary modes near *ca*. 315 Ma and *ca*. 330 Ma (Figure 6C). In both Rewan Group units, the *ca*. 200–400 Ma interval dominates the spectra, but the relative balance within that interval differs between the two formations. In the grouped percentage summary, 28.5% of grains from the Sagittarius Sandstone fall within the 220–285 Ma bin and 55.9% within the 285–400 Ma bin, whereas grains from the Arcadia Formation fall at 52.2% and 40.6%, respectively (Table 2). The Arcadia Formation contains a larger younger Triassic component, whereas the Sagittarius Sandstone retains a larger older Palaeozoic component.

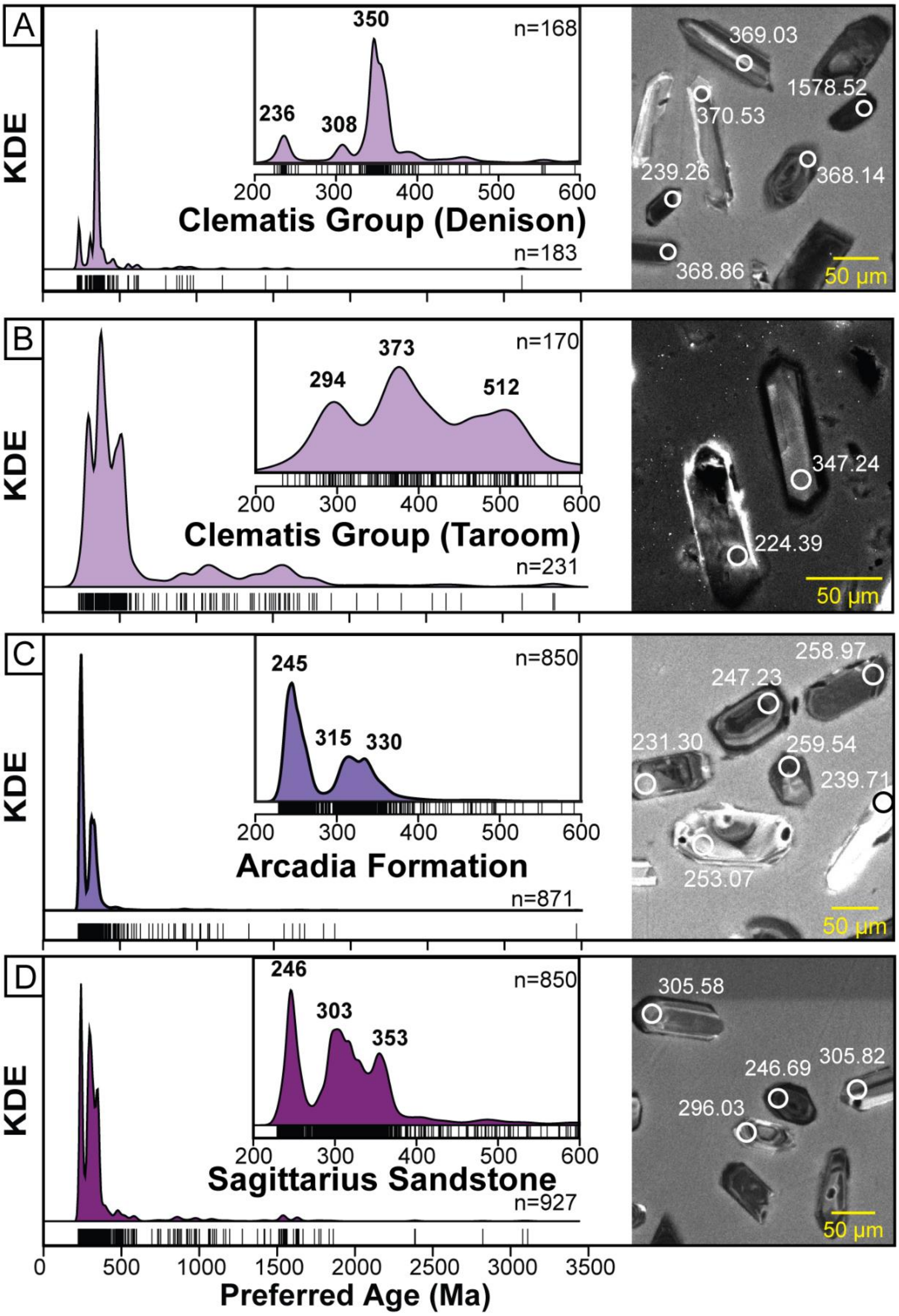

Figure 6. *Kernel density estimates (KDEs) show preferred U–Pb age distributions for (A) Clematis Group (Denison Trough), (B) Clematis Group (Taroom Trough), (C) Arcadia Formation (basin-wide), and (D) Sagittarius Sandstone (Sst.; basin-wide). Insets highlight the <600 Ma portion of each spectrum. Tick marks show individual analyses; n shows the number of grains plotted and inset n values refer to grains younger than 600 Ma. Cathodoluminescence images adjacent to each KDE show representative zircon grains from the corresponding sample group, illustrating typical internal zoning, and spot locations used for U–Pb analyses and their corresponding ages (in Ma).*

The Clematis Group in the Denison Trough is dominated by a mode near ca. 350 Ma with a smaller component near ca. 308 Ma and a minor Triassic component near ca. 236 Ma (Figure 6A). The Clematis Group in the Taroom Trough is characterised by modes near ca. 294 Ma, ca. 373 Ma, and ca. 512 Ma, and it lacks a dominant Triassic mode comparable to the Rewan Group (Figure 6B). This difference is also expressed in the grouped percentages. Only 6.5% of the grains from the Clematis Group in the Taroom Trough fall within the 220–285 Ma bin, and 55.8% are older than 400 Ma. The Clematis Group in the Denison Trough is less extreme: 12.0% of grains fall within the 220–285 Ma bin and 72.1% within the 285–400 Ma bin (Table 2).

Lag-time plots (crystallisation age minus depositional age) also differ between the Rewan Group and the Clematis Group (Figure 7B). Rewan Group curves rise steeply at low lag values, whereas Clematis Group curves rise more gradually and extend further into longer lag times. Because the depositional constraints are MDAs, these lag values represent lower bounds on the true lag time.

Between-sample similarity was evaluated using multidimensional scaling (MDS) derived from a Wasserstein-2 dissimilarity matrix (Figure 9A). Most Sagittarius Sandstone and Arcadia Formation samples plot close together and overlap in MDS space (Figure 9A). Clematis Group samples plot away from this main Rewan Group cluster (Figure 9A).

MDA are summarised using multiple estimators (Table 3). Rewan Group MLA estimates fall within the Triassic and differ among sample groups. Arcadia Formation samples yield MLA estimates that fall in a narrow range of *ca.* 239–236 Ma (Table 3). Sagittarius Sandstone samples show a wider spread in MLA estimates, with samples from the Denison Trough yielding MLA estimates of *ca.* 238–233 Ma and samples from the Taroom Trough and Brumby Plains 1 yielding older MLA estimates, including BP1-24-02 at 244.43 ± 1.55 Ma and BP1-24-03 at 250.2 ± 2.3 Ma (Table 3). For the Clematis Group, the Denison Trough sample

(CT-24-01) yields an MLA estimate of 227.1 ± 6.1 Ma and retains a minor Triassic component, whereas the Taroom Trough sample (T14-25-07) contains few Triassic grains and is dominated by older Palaeozoic ages (Figure 6A, B; Table 3). Across samples, YSG estimates are typically younger than multi-grain estimators and MLA, so all estimators are reported together to document estimator spread and to enable direct comparison among samples (Table 3).

Table 2. *Percentage and grain-count summary of broad detrital zircon age populations for the Sagittarius Sandstone, Arcadia Formation, and Clematis Group composites shown in Figure 6. Values are based on concordant grains only, with counts in parentheses. The table provides a simplified comparison of relative age-population abundance among the four composite spectra.*

Age population	Sagittarius Sandstone (n=927)	Arcadia Formation (n=871)	Clematis Group, Taroom Trough (n=231)	Clematis Group, Denison Trough (n=183)
Hunter Bowen Orogeny (220-<285 Ma)	28.5 % (264)	52.2 % (455)	6.5 % (15)	12.0 % (22)
New England Orogen (285-<400 Ma)	55.9 % (518)	40.6 % (354)	32.9 % (76)	72.1 % (132)
Older Tasmanides (400-<500 Ma)	4.6 % (43)	2.5 % (22)	21.6 % (50)	6.6 % (12)
Pacific-Gondwana (500-<650 Ma)	2.7 % (25)	1.1 % (10)	13.0 % (30)	3.8 % (7)
Grenville Orogen (850-<1250 Ma)	3.1 % (29)	1.7 % (15)	9.5 % (22)	3.8 % (7)
North Australian Craton (1450-<1950 Ma)	3.2 % (30)	0.7 % (6)	8.7 % (20)	0.5 % (1)
Older cratonic grains (1950-3500 Ma)	0.9 % (8)	0.1 % (1)	3.0 % (7)	0.0 % (0)
Unassigned / other	1.1 % (10)	0.9 % (8)	4.8 % (11)	1.1 % (2)

5. Discussion

5.1 Provenance of the Northern Bowen Basin

5.1.1 Sandstone Petrography

Across the succession, most samples plot along the quartz–lithic side of the diagram and feldspar is generally minor (Figure 3). Feldspar-poor compositions are therefore treated as supportive, but not diagnostic, of limited input from fresh feldspar-rich plutonic sources. The main petrographic change is an up-section shift from lithic-rich Blackwater Group and Rewan Group sandstones to more quartz-rich, but still feldspar-poor, Clematis Group sandstones.

Late Permian Blackwater Group samples show that feldspar-poor, lithic-rich compositions were already established before deposition of the Triassic succession (Figure 3A-B, 4A; Michaelsen & Henderson, 2000). Their overlap with Rewan Group QFL fields may reflect continued erosion from similar source rocks, recycling of older basin fill, or both. Petrography alone does not distinguish between those alternatives.

Rewan Group sandstones are likewise feldspar poor but extend to lower-quartz and higher-lithic compositions, consistent with volcaniclastic-rich Rewan Group petrofacies (Figure 3C, D; Table 1; Bashari, 2000; Michaelsen & Henderson, 2000). A subset of Sagittarius Sandstone samples from Theodore NS150 is compositionally distinct and plots at very low quartz with elevated feldspar and volcanic lithic contents relative to the rest of the Rewan Group (Figure 4B). Grech (2001) interpreted comparable feldspar-rich, tuffaceous beds there as syndepositional volcanic input. Its position on the eastern margin of the Taroom Trough is consistent with that interpretation, although local ash-fall reworking and facies-controlled concentration remain viable alternatives.

Clematis Group samples record the clearest up-section petrographic shift. They are more quartz rich, remain feldspar poor, and plot mainly in quartzose to transitional recycled fields, consistent with previous descriptions of the unit (Figure 3E-F; Kassan, 1994). The change is therefore not from lithic-rich to feldspathic sandstones, but from lithic-rich, feldspar-poor sandstones to more quartz-rich, still feldspar-poor sandstones. Comparable up-section shifts towards more quartz-rich and recycled compositions have been described in other retroarc foreland basins and are commonly linked to changes in source access, recycling, and drainage organisation (DeCelles & Burden, 1992; Dutta & Wheat, 1993; Gómez et al., 2019; Maravelis et al., 2023).

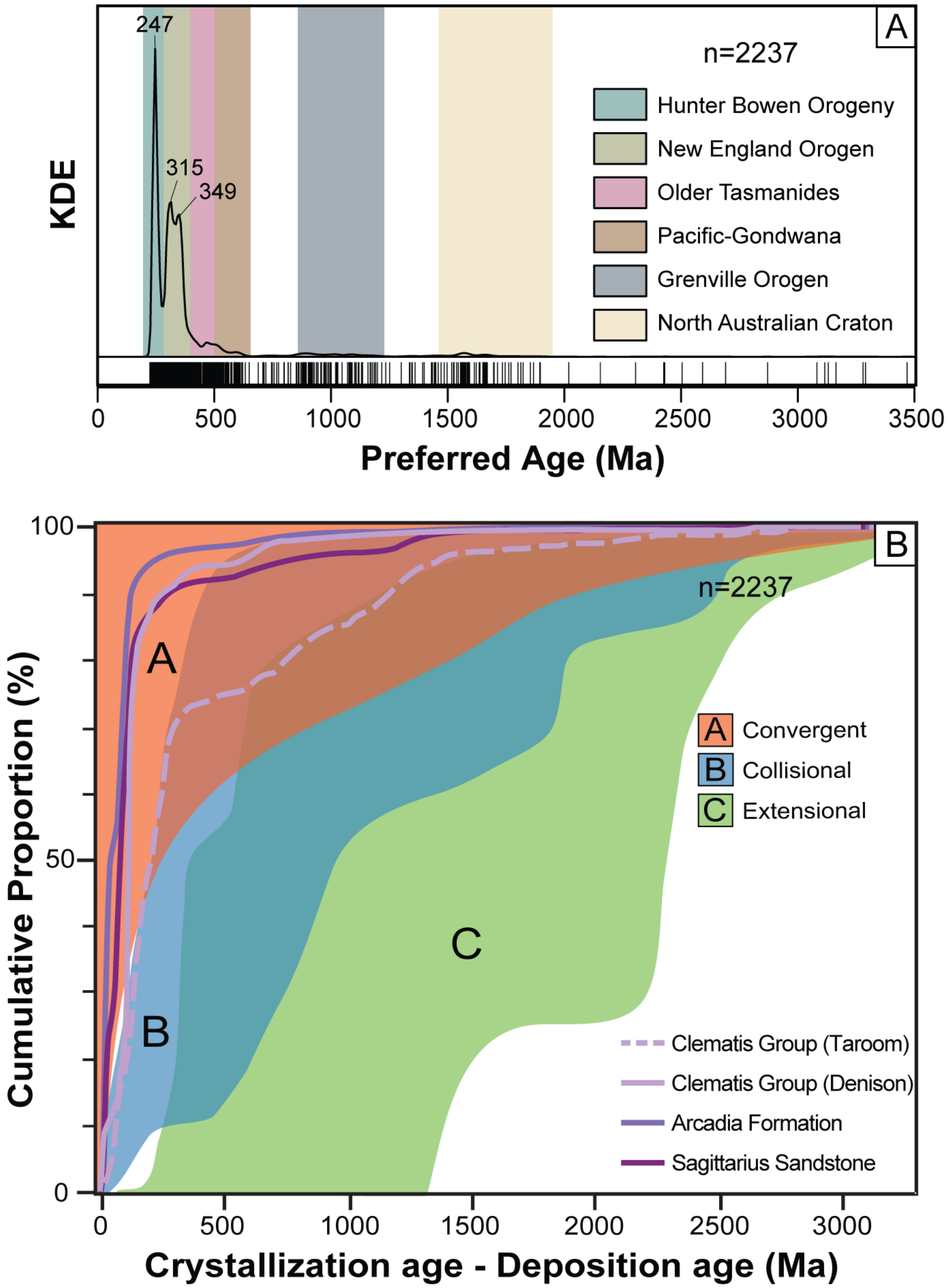

Figure 7. *(A) Kernel density estimate (KDE) of preferred U–Pb ages for all concordant detrital zircon analyses from this study (*n *= 2212), with shaded bands indicating broad age domains commonly associated with regional source terranes and tectonic provinces (Hunter–Bowen/New England Orogen, older Tasmanides, Pacific–Gondwana, Grenville, and North Australian craton). (B) Cumulative proportion plot of crystallisation age minus depositional age (lag time) for individual samples, modified after the conceptual framework of Cawood et al. (2012) to illustrate relative contributions from convergent-margin, collisional, and extensional source settings.*

5.1.2 Detrital Zircon Geochronology

Detrital zircon age spectra from Triassic sandstones in the northern Bowen Basin are dominated by Permian–Triassic and Carboniferous populations (Figures 6 and 7A). When Rewan Group samples are pooled, the dataset is characterised by three principal modes at ca. 245 Ma, 312 Ma, and 341 Ma (Figure 7A), consistent with sustained sediment supply from the active Tasmanide margin with subordinate contributions from older terranes from the east. The Sagittarius Sandstone and Arcadia Formation share the same main age populations, but they are not identical. The Sagittarius Sandstone retains stronger older Palaeozoic modes, whereas the Arcadia Formation is more strongly dominated by its ca. 245 Ma Triassic peak (Figure 6C, D; Table 2). The Arcadia Formation's provenance is therefore more strongly dominated by the younger Triassic population, whereas the Sagittarius Sandstone retains a larger older Palaeozoic component. In MDS space, most Sagittarius Sandstone and Arcadia Formation samples occupy the same Rewan Group field, but the Sagittarius Sandstone spans a broader range of positions (Figure 9A), indicating greater internal variability. The percentage data show a stronger relative contribution from the younger population in the Arcadia Formation, but they do not by themselves measure absolute volcanic flux.

The dominant Middle Triassic zircon component in the Rewan Group is most simply explained by derivation from margin-proximal igneous sources associated with the Permian–Triassic magmatic belt of the New England Orogen and related arc-to-retroarc systems (Figure 7A). This interpretation is consistent with the feldspar-poor, lithic-rich petrography of the Rewan Group. Together, the DZ spectra and QFL data indicate substantial input from eastern, margin-proximal sources, including contemporaneous volcanic and volcanic–plutonic material during Rewan Group deposition.

Carboniferous–Permian and older Palaeozoic zircon components require contributions from older Tasmanide source rocks and/or multicycle sediment pathways. These age ranges

No.	Sample	Formation	Location	Literature	YSG (±2σ) (Ma)	YGC (±2σ) (Ma)	MLA (±2σ) (Ma)
1	WM1-D6	Moolayember Formation	Bowen Basin	Sobczak et al., 2022	219.4 ± 7.1	245.7 ± 1.7; MSWD 0.77; 26 grains	236.7 ± 3.7
2	364	Moolayember Formation	Bowen Basin	Sobczak et al., 2022	183.5 ± 4.4	233.9 ± 0.9; MSWD 1.55; 6 grains	200.8 ± 4.8
3	363	Moolayember Formation	Bowen Basin	Sobczak et al., 2022	217.7 ± 1.5	234.1 ± 1.6; MSWD 0.80; 3 grains	220.0 ± 1.8
4	BDT2	Clematis Group	Bowen Basin	Adams et al., 2022	248.0 ± 4.3	265.2 ± 1.0; MSWD 1.1; 5 grains	261.5 ± 21.0
5	T14-25-07*	Clematis Group	Bowen Basin	This study	233.06 ± 4.3	237.8 ± 4.1; MSWD 0.2; 3 grains	238.5 ± 8.1
6	CT-24-01*	Clematis Group	Bowen Basin	This study	223.83 ± 6.9	229.3 ± 3.8; MSWD 1.7; 7 grains	227.1 ± 6.1
7	ES-23-22*	Arcadia Formation	Bowen Basin	This study	233.89 ± 4.7	247.3 ± 2.5; MSWD 1.01; 6 grains	236.7 ± 3.7
8	CT-23-31*	Arcadia Formation	Bowen Basin	This study	231.48 ± 5.6	237.0 ± 1.0; MSWD 1.6; 15 grains	239.5 ± 2.7
9	ES-23-31*	Arcadia Formation	Bowen Basin	This study	229.26 ± 10.3	236.2 ± 2.1; MSWD 0.82; 13 grains	239.2 ± 3.2
10	DW-24-03*	Arcadia Formation	Bowen Basin	This study	228.50 ± 6.2	233.2 ± 1.3; MSWD 0.77; 24 grains	235.8 ± 2.1
11	T14-25-09*	Arcadia Formation	Bowen Basin	This study	230.52 ± 4.3	234.9 ± 1.2; MSWD 0.64; 18 grains	237.7 ± 1.7
12	RW1-24-03*	Sagittarius Sandstone	Bowen Basin	This study	230.79 ± 7.3	236.7 ± 1.3; MSWD 1.1 ; 14 grains	237.7 ± 2.5
13	RW1-24-07*	Sagittarius Sandstone	Bowen Basin	This study	230.17 ± 4.8	234.3 ± 1.1; MSWD 1.2; 27 grains	233.3 ± 2.1
14	NEBO1	Sagittarius Sandstone	Bowen Basin	Adams et al., 2022	244.0 ± 3.0	249.7 ± 2.5; MSWD 1.3; 6 grains	248.0 ± 6.6
15	D27-25-01*	Sagittarius Sandstone	Bowen Basin	This study	242.48 ± 5.8	246.7 ± 1.4; MSWD 0.61; 18 grains	246.0 ± 1.9
16	BP1-24-03*	Sagittarius Sandstone	Bowen Basin	This study	241.11 ± 6.0	247.8 ± 1.5; MSWD 0.98; 22 grains	250.2 ± 2.3
17	BP1-24-02*	Sagittarius Sandstone	Bowen Basin	This study	236.09 ± 5.9	242.1 ± 1.5; MSWD 1.07; 17 grains	244.43 ± 1.6
18	BURRA1	Warang Sandstone	Northeastern Galilee Basin	Adams et al., 2022	259.0 ± 4.0	275.8 ± 2.4; MSWD 0.98; 8 grains	274.2 ± 3.2
19	Warang Top	Warang Sandstone	Northeastern Galilee Basin	Todd et al., 2022	244.6 ± 4.9	276.4 ± 2.6; MSWD 1.15; 6 grains	246.6 ± 11.4
20	WSS0409	Warang Sandstone	Northeastern Galilee Basin	Todd et al., 2022	265.5 ± 5.0	273.9 ± 4.7; MSWD 1.15; 6 grains	280.6 ± 8.9
21	H6B38	Warang Sandstone	Northeastern Galilee Basin	Todd et al., 2022	232.0 ± 2.5	280.4 ± 3.8; MSWD 1.04; 5 grains	232.0 ± 7.4
22	H6B26	Warang Sandstone	Northeastern Galilee Basin	Todd et al., 2022	247.6 ± 3.1	272.4 ± 3.8; MSWD 2.03; 3 grains	248.0 ± 7.5
23	WSS2908	Warang Sandstone	Northeastern Galilee Basin	Todd et al., 2022	242.7 ± 3.9	274.1 ± 3.8; MSWD 1.04; 5 grains	244.5 ± 9.1
24	H6B47	Porcupine Gorge Formation	Northeastern Galilee Basin	Todd et al., 2022	223.4 ± 10.7	238.7 ± 3.0; MSWD 0.30; 3 grains	236.9 ± 5.2
25	PGF01	Porcupine Gorge Formation	Northeastern Galilee Basin	Todd et al., 2022	228.0 ± 3.0	229.5 ± 1.8; MSWD 1.79; 3 grains	228.2 ± 3.3
26	GPC_C	Bandanna Formation	Southern Galilee Basin	Philips et al., 2017	233.0 ± 13	247.4 ± 1.9; MSWD 0.75; 43 grains	249.6 ± 4.1
27	BR15	Brooweena Formation	Northern Gympie Terrane	Rosenbaum et al., 2020	242.3 ± 11.0	252.6 ± 1.9; MSWD 1.9; 24 grains	249.3 ± 6.1
28	BR03	Brooweena Formation	Northern Gympie Terrane	Rosenbaum et al., 2020	237.3 ± 8.1	245.3 ± 2.3; MSWD 0.9; 10 grains	247.5 ± 3.8
29	BR07	Brooweena Formation	Northern Gympie Terrane	Rosenbaum et al., 2020	275.5 ± 12.0	285.4 ± 4.8; MSWD 2.1; 5 grains	305.6 ± 3.3
30	TE21	Teebar Formation	Northern Gympie Terrane	Rosenbaum et al., 2020	243.0 ± 11.0	253.7 ± 1.1; MSWD 0.5; 65 grains	257.6 ± 1.0
31	TE26	Teebar Formation	Northern Gympie Terrane	Rosenbaum et al., 2020	233.0 ± 11.0	245.6 ± 2.9; MSWD 0.5; 16 grains	254.9 ± 1.2
32	GY-13-10	Kin Kin Beds	Southern Gympie Terrane	Li et al., 2015	224.0 ± 10.6	229.9 ± 2.9; MSWD 1.1; 10 grains	231.1 ± 5.0
33	GY-13-34	Kin Kin Beds	Southern Gympie Terrane	Li et al., 2015	225.4 ± 9.6	230.7 ± 4.9; MSWD 0.9; 3 grains	238.5 ± 3.6
34	GYM36	Keefton Formation	Southern Gympie Terrane	Adams et al., 2022	244.0 ± 6.0	249.7 ± 1.6; MSWD 1.1; 13 grains	250.6 ± 1.87
35	GY-13-31	Keefton Formation	Southern Gympie Terrane	Li et al., 2015	249.9 ± 10.4	256.3 ± 6.9; MSWD 1.5; 4 grains	252.9 ± 9.4
36	GY-13-07	Tamaree Formation	Southern Gympie Terrane	Li et al., 2015	235.9 ± 5.6	241.3 ± 2.2; MSWD 0.7;16 grains	244.8 ± 4.7
37	GY-13-11	Tamaree Formation	Southern Gympie Terrane	Li et al., 2015	242.9 ± 9.0	250.3 ± 1.7; MSWD 1.0; 30 grains	250.4 ± 2.0

Table 3. *Summary of detrital zircon age data and maximum depositional age estimates from this study and from compiled previous studies.*

are common within the broader Tasmanide orogenic belt and can also be introduced through recycling of late Palaeozoic basin fill. Recycling is viable in the Bowen Basin because contractional deformation and structural reactivation affected the Permian–Triassic succession, generating local uplift and erosion that could remobilise older sedimentary packages (Korsch et al., 2009). Minor Proterozoic zircon populations occur across the dataset (Figure 7A), consistent with limited cratonward input and/or recycling from older successions. At the scale resolved by DZ alone, the older component does not uniquely distinguish between direct erosion of exposed basement provinces and recycling through Permian sedimentary successions.

The clearest shift from the Rewan Group occurs in the Clematis Group of the Taroom Trough. Its spectrum lacks the dominant *ca*. 240–250 Ma peak that characterises the Rewan Group and is instead dominated by older Palaeozoic modes at ca. 294, 373, and 512 Ma (Figure 6B). The grouped percentages show the same pattern, with only 6.5% of grains from the Clematis Group in the Taroom Trough falling in the 220–285 Ma bin, whereas 55.8% are older than 400 Ma (Table 2). The Clematis Group in the Denison Trough is less extreme. It retains a minor *ca*. 236 Ma component but is dominated by the 285–400 Ma population, which accounts for 72.1% of its grains (Figure 6A; Table 2). This shift is consistent with the more quartzose, feldspar-poor petrography of the Clematis Group. In MDS space, Clematis Group samples span a wider range and include points displaced from the Rewan Group cluster (Figure 9A). Clematis Group lag curves show a lower proportion of short crystallisation–deposition age gaps than the Rewan Group (Figure 7B), using MLA-based MDAs as the depositional reference. Overall, these data support reduced near-depositional arc input and greater contributions from older sources, although recycling remains a competing explanation. This contrast motivates the next step in interpretation, in which palaeodrainage and sediment-routing models are evaluated against the spatial structure of the DZ dataset and the basin framework.

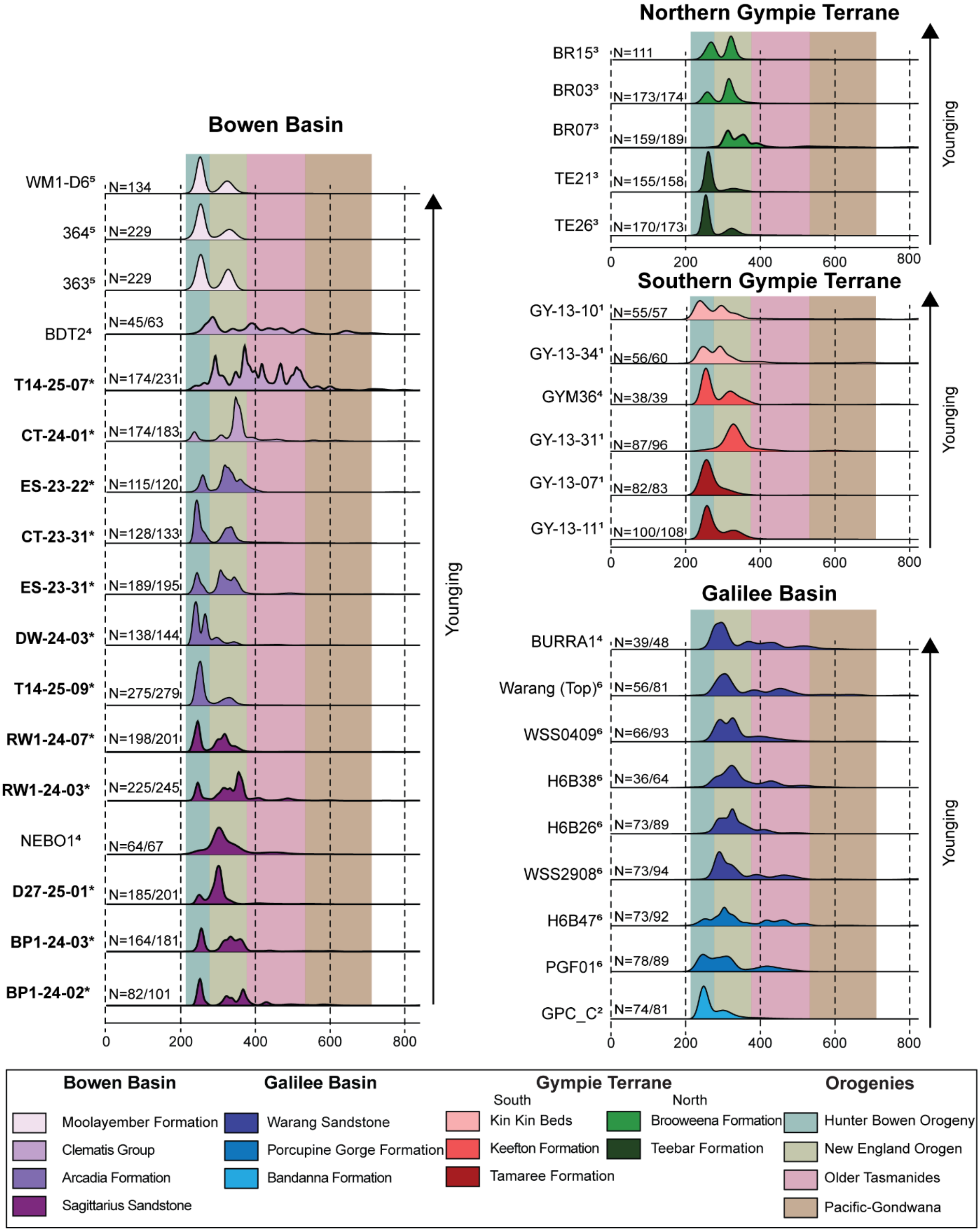

Figure 8. *Kernel density estimates (KDEs) show preferred U–Pb age distributions (<800 Ma) for Triassic samples from the Bowen Basin (this study and published datasets), the Galilee Basin, and the northern and southern Gympie Terrane. Samples are ordered by stratigraphic younging within each region; * denotes samples analysed in this study. References:* ***1*** *= Li et al. (2015);* ***2*** *= Phillips et al. (2017);* ***3*** *= Rosenbaum et al. (2020);* ***4*** *= Adams et al. (2022);* ***5*** *= Sobczak et al. (2022);* ***6*** *= Todd et al. (2022). N shows the number of grains plotted relative to the total number of concordant grains. Shaded vertical bands indicate broad age domains associated with regional Tasmanide and cratonward source provinces (see legend).*

5.2 Sediment routing and palaeodrainage implications

Detrital zircon age distributions can be used as basin-scale sediment-routing tracers because mixtures of age populations preserve information about catchment integration, recycling, and along-strike mixing that can be compared quantitatively between depocentres (Mason et al., 2022; Romans et al., 2016; Shaanan et al., 2018; Shaanan & Rosenbaum, 2018). However, robust routing interpretations require integration of DZ results with independent sediment-transport constraints, particularly palaeocurrent indicators and basin architecture, following the approach used in comparable source-to-sink studies (e.g., Tucker et al., 2016). Here, pairwise spectral dissimilarity is quantified using the Wasserstein-2 distance and visualised with multidimensional scaling (MDS; Figure 9A). Samples that plot close together have similar age distributions, whereas those farther apart are more dissimilar. Axis values are not interpreted directly; instead, similarity is evaluated against the palaeodrainage reconstruction and within-basin KDE structure (Figures 6, 7, 10).

For the Rewan Group, palaeodrainage indicates dominant input from the eastern margin, with minor western and northwestern contributions routed into trough-confined axial systems (Figure 10A). This geometry is consistent with an integrated Rewan Group system. Sagittarius Sandstone and Arcadia Formation samples plot closely in MDS space and show similar KDE structures dominated by Permian–Triassic and Late Carboniferous populations (Figures 6C–D, 7A, 9A). Both units are dominated by the 220–400 Ma interval, although the Arcadia Formation contains a stronger younger component than the Sagittarius Sandstone. These data indicate that the Rewan Group depositional system remained dominated by eastern active-margin input, but that the balance between younger and older Palaeozoic populations varied within the basin. The Carboniferous component may have been derived from northern provinces such as the Charters Towers Province or Connors Subprovince, and from western sources such as the Anakie Province (Figure 10; Jell, 2013). These assignments are not unique, and zircon ages alone do not distinguish direct erosion from recycling. The high proportion of short crystallisation–deposition age gaps in the Rewan dataset (Figure 7B) is consistent with continued delivery from an active convergent margin source, rather than exclusive recycling of older basin fill.

Although the Rewan Group samples are broadly coherent, the routing system was not spatially uniform. BP1-24-02 is the clearest Rewan Group offset in Figure 9A, and BP1-24-03 trends in the same direction but less strongly. Relative to the tighter Arcadia Formation cluster and several Sagittarius Sandstone samples, these spectra retain the Triassic peak but contain stronger older Palaeozoic components (Figure 8). This part of ordination space is therefore interpreted as an inferred shift from strongly Triassic-dominated spectra towards mixed spectra with a larger older Palaeozoic contribution. This interpretation is based on the KDE structure rather than on the axis alone. In the context of Figure 10A, this behaviour is consistent with local mixing where east-derived sediment entered trough-confined axial systems and interacted with sediment delivered from surrounding cratonward terranes. The palaeodrainage model includes minor sediment inputs from the western and northwestern margins (Figure 10A), which provide plausible pathways for introducing older zircon components without requiring a basin-wide change in the dominant source. Structural segmentation into troughs and intervening highs likely focused axial transport but allowed episodic transverse inputs (Brakel et al., 2009; Danis et al., 2012; Korsch, Totterdell, Fomin, et al., 2009). This spatial context also affects recycling potential. Chronostratigraphic constraints indicate more continuous Triassic accumulation in the Taroom Trough than in the Denison Trough, where non-deposition and/or erosion is more likely across the Permian–Triassic transition (Scipione et al., 2026). Where the stratigraphic record is condensed, older units are more likely to be exposed and available for recycling.

Clematis Group samples record a change in routing relative to the Rewan Group, but the signal varies by depocentre. The palaeodrainage reconstruction suggests reduced east-derived supply and greater input from western and northwestern continental-interior terranes during Clematis Group deposition (Figure 10B). The provenance signal supports this inference. T14-25-07 is separated from the main Rewan Group field in MDS space (Figure 9A) and shows a distinct KDE structure relative to the Rewan Group, with reduced Permian–Triassic peaks and greater older Palaeozoic contributions (Figure 6B–D). The Clematis Group in the Taroom Trough is markedly older-weighted than the Rewan Group, whereas the Clematis Group in the Denison Trough composite is more intermediate. These differences are consistent with increased cratonward input and/or recycling, strongest in the Taroom Trough rather than uniformly across the basin. Potential sources for older Tasmanide-age grains include the Thomson Basement and recycled Drummond Basin sediments (Figure 10B; Jell, 2013). In lag-time space, the dataset from the Clematis Group also shifts towards older crystallisation–deposition offsets (Figure 7B), consistent with increased input from older crustal sources and/or multicycle recycling. Because recycling can generate similar spectral shifts, routing interpretations should be tested against structural position, proximity to unconformities, and additional sampling across depocentres. This shift can be tested against three alternatives, namely catchment expansion, basin tilting and drainage capture, or increased recycling within the basin fill. Their relative importance may vary along the troughs.

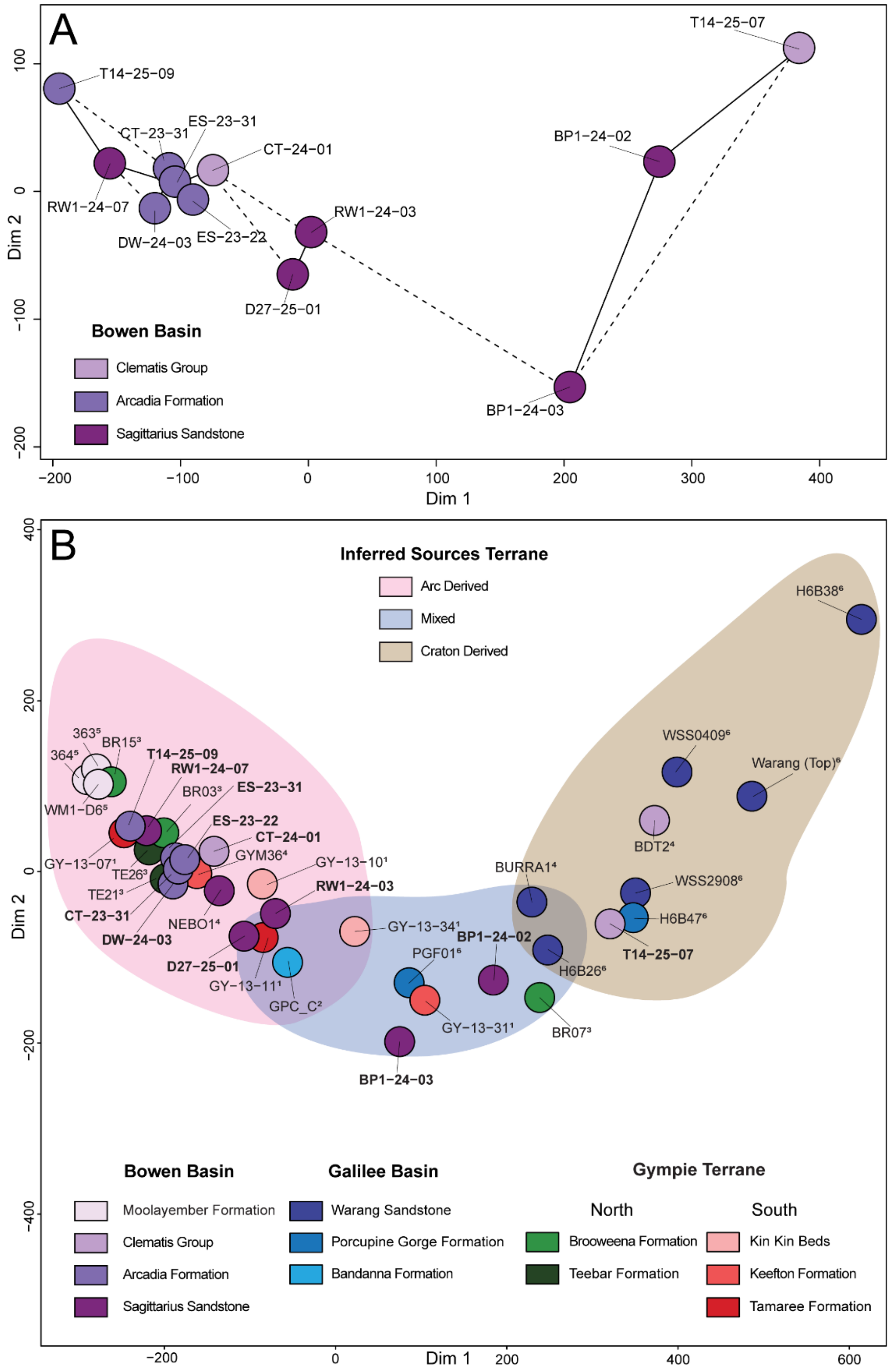

Figure 9. *Multidimensional scaling (MDS) plots based on pairwise Wasserstein-2 distances calculated from detrital zircon age distributions. Distances are visualised in two dimensions, where closer points indicate more similar age spectra. Dim 1 and Dim 2 are unitless ordination axes and are not interpreted as direct geological variables. (A) MDS for samples analysed in this study, coloured by stratigraphic unit. (B) MDS including this study, shown in bold type, and published datasets from the Bowen Basin, Galilee Basin, and northern and southern Gympie Terrane. Polygons outline inferred arc-dominated, mixed, and craton-dominated fields (colour scheme as in Figure 8).* ***1*** *= Li et al. (2015);* ***2*** *= Phillips et al. (2017);* ***3*** *= Rosenbaum et al. (2020);* ***4*** *= Adams et al. (2022);* ***5*** *= Sobczak et al. (2022);* ***6*** *= Todd et al. (2022).*

5.3 Tectonic implications

Rewan Group sandstones include a large fraction of zircons with short crystallisation–deposition age gaps (Figure 7B), consistent with near-depositional input. The dominance of Middle Triassic components in Sagittarius Sandstone and Arcadia Formation spectra (Figure 6C–D) and in the basin-wide KDE (Figure 7A) is consistent with continued convergent-margin magmatism and tectonism along the Tasmanide margin during the Triassic (Jessop et al., 2019; P. Li et al., 2012; Rosenbaum et al., 2020, 2025). Rosenbaum (2026) interpreted the New England Orogen as a Middle Permian–Late Triassic continental arc dominated by calc-alkaline felsic igneous rocks, mainly I-type granitoids, with major magmatic activity beginning at ~270 Ma, peaking at ~252 Ma, and continuing into the Late Triassic. Hf-isotope data from granitoids of the Permian–Triassic New England Batholith are consistent with this interpretation and indicate juvenile magmatic input mixed with evolved crustal components in arc-related magmas (Phillips et al., 2011; Shaw et al., 2011). Regional detrital zircon datasets extend that pattern beyond the exposed batholith. Tucker et al. (2016) reported a relatively continuous Triassic–Cretaceous zircon record from eastern Australia with dominantly positive epsilon Hf (εHf) values. Foley et al. (2021) showed that Triassic–Jurassic detrital zircons from eastern Gondwana are likewise dominated by positive εHf values that overlap New England Orogen continental-arc zircons. Together, these data support interpretation of the *ca*. 230–250 Ma zircon population as derived from a juvenile continental-arc system along the eastern Gondwana margin. They do not distinguish volcanic from plutonic arc sources, but the short crystallisation-to-deposition age gaps provide the clearest evidence for rapid transfer of young detritus into the basin.

The structural framework provides additional context for these provenance trends (Danis et al., 2012; Babaahmadi et al., 2017; Rosenbaum et al., 2025; Scipione et al., 2026). Chronostratigraphic constraints indicate earlier and more continuous Triassic accumulation in the Taroom Trough than in the Denison Trough, with a longer interval of non-deposition and/or erosion in the backbulge (Scipione et al., 2026). Such partitioning is expected in a retroarc foreland basin where flexural subsidence and intrabasinal structures focus accommodation in some depocentres while other areas experience bypass or condensation (Korsch, Totterdell, Fomin, et al., 2009). Despite this segmentation, most Rewan Group samples retain similar age mixtures across sampled depocentres, implying basin-scale dispersal of arc-derived detritus during this stage. The offset position of BP1-24-02 suggests local variation in sediment mixing within the Taroom Trough.

The Clematis Group shift is strongest in the Taroom Trough, where older Palaeozoic components become more prominent and short-lag Triassic input declines. One mechanism is deformation-driven drainage reorganisation and inversion, which can expose older successions to erosion, alter gradients, and reroute sediment pathways (Korsch, Totterdell, Cathro, et al., 2009). Triassic unconformities and changes in basin fill indicate that provenance shifts may reflect changes in sediment routing and recycling, rather than just a change in source (Brakel et al., 2009). Reduced accommodation and uplift of intrabasinal highs and backbulge areas can expose older basin fill to erosion, increase recycling, and dilute the arc-derived signal. The Clematis Group signal in the Taroom Trough is consistent with this mechanism and with increased continental-interior input during later Triassic basin evolution.

These competing explanations can be tested by sampling additional depocentres: basin-wide reduction in arc supply versus local rerouting and recycling. If the arc supply decreased across the whole basin, the Clematis Group spectra should show a similar drop in the Early Triassic population everywhere. If the change reflects rerouting and recycling, the magnitude of the shift should vary with structural position and with proximity to unconformities and inversion features (Babaahmadi et al., 2021; Korsch, Totterdell, Fomin, et al., 2009; Sliwa et al., 2018). Further discrimination would benefit from additional provenance tracers, such as zircon Hf isotopes and trace-element chemistry.

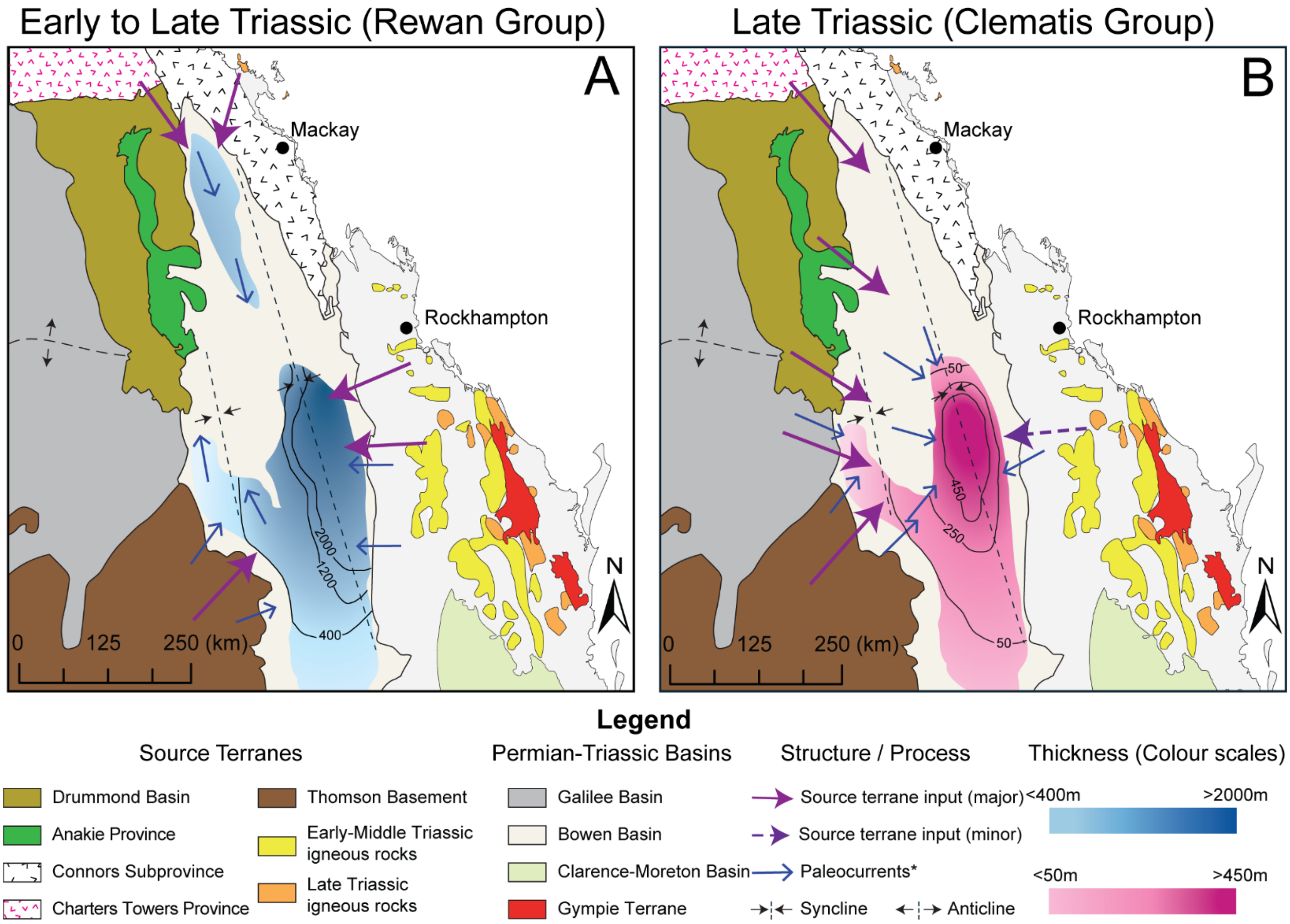

Figure 10. *Maps show inferred sediment-transport pathways, potential source terranes, and isopach (thickness) trends for (A) the Rewan Group and (B) the Clematis Group. Blue arrows show compiled palaeocurrent directions. Purple arrows show interpreted source-terrain inputs; solid arrows denote major inputs and dashed arrows denote minor inputs. Thickness contours highlight the main depocentres. Potential source regions include the Thomson Basement, Drummond Basin, Anakie Province, Charters Towers Province, and Connors Subprovince. Palaeocurrent data are compiled from Jensen (1975), Kassan (1994), and Grech (2001).*

5.4 Regional comparison and basin-to-basin connectivity

Inter-basin comparison of Triassic detrital zircon age distributions provides an empirical test of provenance similarity when evaluated against stratigraphic and sediment-transport constraints. Age spectra are compared using KDEs and similarity is evaluated using MDS of Wasserstein-2 distances (Figures 8, 9B). The polygons in Figure 9B outline interpretive arc-dominated, mixed, and craton-dominated fields and are used as summaries of regional similarity structure rather than exact matches.

The inferred arc-dominated field contains spectra dominated by Permian–Triassic and Carboniferous components and captures the Rewan Group-like signal defined within the Bowen Basin (Figures 6C–D, 8, 9B). Many Gympie Terrane samples and the Bandanna Formation plot in this field, indicating access to a similar zircon-producing source spectrum (Li et al., 2015).

The inferred mixed and craton-dominated fields are older-weighted than the arc-dominated field. The Clematis Group sample from the Taroom Trough plots with older-weighted Galilee Basin Triassic samples, including the Warang Sandstone and Porcupine Gorge Formation, consistent with reduced young arc input and greater contributions from older sources (Figures 8, 9B). Todd et al. (2022) place the Porcupine Gorge Formation and Warang Sandstone broadly within the same Middle–Late Triassic interval as Clematis Group deposition, within the uncertainty of MDA-based correlation. CT-24-01 is more intermediate and retains a minor Permian–Triassic peak, although its spectrum is dominated by Carboniferous ages (Figure 6A).

Moolayember Formation reference spectra plot within the arc-dominated field and show renewed prevalence of younger zircon modes, but stratigraphic uncertainty means that comparison remains supportive rather than definitive (Figures 8, 9B). Used this way, the regional comparison helps distinguish shared source access from integrated routing pathways when similarity patterns are evaluated against basin architecture and palaeocurrent constraints.

5.5 Implications for provenance interpretations in other basins

Source-to-sink studies treat the sedimentary system as a connected network linking source, transfer, and sink (Castelltort et al., 2023; Mason et al., 2022; Romans et al., 2016). In deep-time settings, provenance data help test whether stratigraphic change reflects rerouting, recycling, storage, or differential preservation. In the Bowen Basin, the Rewan Group–Clematis Group transition records such a signal through shifts in detrital zircon spectra, maximum depositional ages, QFL petrography, and stratal architecture. These changes support a routing shift, but they do not isolate a single driver or quantify sediment flux through the full source-to-sink system. Within the Hunter–Bowen Orogeny, a subduction-related convergent-margin system along eastern Gondwana, this framework shows that combining detrital-zircon data, petrography, palaeocurrents, and stratigraphy can be used to test changes in sediment routing across connected basin settings. At a regional scale, this approach helps evaluate provenance and basin reorganisation from the arc-proximal Gympie Terrane, through the retroarc foreland Bowen Basin, to the cratonward Galilee Basin.

Sorting and recycling remain viable alternatives because both can modify zircon spectra without requiring a new source terrane. Hydraulic sorting can bias the youngest part of the zircon spectrum, so it is treated as a possible secondary control. Sorting alone, however, is unlikely to explain the Clematis Group signal, which also includes stronger older Palaeozoic modes, more quartzose petrography, and longer crystallisation-to-deposition age gaps (Carraro et al., 2024; DeGraaff-Surpless et al., 2003; Sylvester et al., 2022). A real change in sediment supply is therefore preferred, with sorting and sampling bias acting as subordinate modifiers.

Signal preservation depends on buffering, delay, and overprinting during transfer and deposition, and on whether autogenic variability obscures the primary pattern (Mason et al., 2022; Romans et al., 2016). Robust interpretation therefore requires enough samples and sufficient chronostratigraphic control to distinguish temporal change from spatial mixing.

Multi-cycle recycling, long transport paths, and along-strike mixing can time-average zircon populations and reduce compositional contrasts, while zircon fertility and lithological targeting can bias spectra towards zircon-rich sources (Dickinson & Gehrels, 2009).

A practical approach is to treat provenance interpretations as testable hypotheses and evaluate them with a multi-proxy dataset that integrates detrital zircon, QFL petrography, palaeocurrent data, and stratigraphic architecture (Tucker et al., 2016). Inter-basin comparisons should use consistent filtering and distance metrics computed from empirical cumulative age distributions. A Wasserstein-2 dissimilarity matrix can then be used to visualise similarity structure (Lipp & Vermeesch, 2022; Vermeesch, 2018). Sampling should be densest across key stratigraphic boundaries and along depositional strike, where routing change and mixing are most likely to vary. Distance-based results should be reported with grain counts and checked for sensitivity to sample size. Recycling-dominated intervals may show broader spectra and longer minimum crystallisation-to-deposition age gaps when MDAs are used as depositional constraints (Cawood et al., 2012). Time-equivalent units should converge in similarity space where correlation and transport constraints support a shared routing network. Similarity alone does not demonstrate sediment transfer.

Conclusion

This study tested how Triassic provenance and sediment routing changed through time in the northern Bowen Basin and how those changes relate to adjacent basins and terranes in eastern Australia.

The results define two contrasting provenance states. Rewan Group sandstones share similar age spectra and occupy the same part of ordination space, indicating a broadly coherent provenance signal across the sampled structural domains. Short minimum lag times and feldspar-poor, lithic-rich petrography are consistent with rapid delivery of margin-derived sediment. By contrast, Clematis Group sandstones, especially in the Taroom Trough, show reduced 220–285 Ma input, more grains older than 400 Ma, and more quartzose petrography. Together with published palaeocurrents, this pattern indicates reduced east-fed arc supply and greater cratonward input and/or recycling during Clematis Group deposition.

Regional comparisons support that interpretation. Rewan Group spectra resemble the Bandanna Formation and Gympie Terrane units, whereas Clematis Group spectra are closer to the Warang Sandstone and Porcupine Gorge Formation. Moolayember Formation reference spectra shift back towards a Rewan Group-like signature, although that comparison remains stratigraphically uncertain.

Overall, provenance and sediment routing in the northern Bowen Basin changed from a relatively coherent margin-derived Rewan Group system to a more mixed Clematis Group system with stronger cratonward and/or recycled input. The main contribution of this study is to define that shift using an integrated dataset of detrital zircon ages, sandstone petrography, and palaeocurrent context, and to place it in a regional comparative framework. It therefore provides a practical basis for testing how provenance-change signals are expressed and modified in retroarc basin systems.

Acknowledgements

We gratefully acknowledge the Geological Survey of Queensland and the team at Zillmere for providing access to the Drake NS27, Taroom 14, Rewan 1 and Theodore NS150. We also acknowledge the use of facilities and technical support from the Queensland Core Library (GSQ, Zillmere). We also thank Santos and Mel Wilkinson for permission to sample the Brumby Plains 1 core, and the landholders at Duckworth Creek, Oaky Creek and Early Storms Creek for access to outcrop localities. We also thank the Department of the Environment, Tourism, Science, and Innovation for access to “The Crater” and Mt. Round in the Seracold State Forest. We respectfully acknowledge the Traditional Owners past, present and emerging of the Country on which this work was conducted, including Bindal, Wulgurukaba, Bidjara, Gayiri, Gabalara, Gangulu and Biri Country.

We are thankful to Huiqing Huang and the AAC staff for their guidance and training with the LA-ICP-MS system and data reduction workflows. M.S. is grateful to the Team of Dreams for insightful tips and discussions on Triassic stratigraphy.

Funding

This work was funded by the James Cook University's College of Science and Engineering Research Fund.

Conflict of interest

The authors declare that they have no known competing financial interests or personal relationships that could have appeared to influence the work reported in this paper.

Data availability statement

The data supporting this study are included in the article and its supplementary material (Supplementary Dataset S1, S2 and S3). Additional information is available from the corresponding author on reasonable request.

References

Adams, C.J., Campbell, H.J., Korsch, R.J. & Griffin, W.L. (2022) Detrital zircons in Triassic–Cretaceous sandstones, Clarence-Moreton Basin, eastern Australia: speculations upon Australia and Zealandia provenances. *Australian Journal of Earth Sciences*, *69*(7), 909–928. https://doi.org/10.1080/08120099.2022.2070277.

Andrade, C., Sobczak, K., Vasconcelos, P., Holl, H.G., Hurter, S. & Allen, C. (2023) U-Pb detrital zircon geochronology of the Middle to Upper Jurassic strata in the Surat Basin: New insights into provenance, paleogeography, and source-sink processes in eastern

Australia. *Marine and Petroleum Geology*, *149*, 106122. https://doi.org/10.1016/J.MARPETGEO.2023.106122.

Asmussen, P. (2020) *INSIGHTS FROM THE DEVONIAN ADAVALE BASIN ON THE TECTONIC HISTORY OF THE THOMSON OROGEN*.

Asmussen, P., Gust, D.A., Bryan, S.E., Purdy, D., Murphy, D. & Allen, C.M. (2023) Multimethod provenance analysis using detrital zircon and rutile U-Pb geochronology across Devonian basin systems in the Tasmanides of eastern Australia. *Gondwana Research*, *118*, 174–191. https://doi.org/10.1016/J.GR.2023.03.004.

Ayaz, S.A., Rodrigues, S., Golding, S.D. & Esterle, J.S. (2016) Compositional variation and palaeoenvironment of the volcanolithic Fort Cooper Coal Measures, Bowen Basin, Australia. *International Journal of Coal Geology*, *166*, 36–46. https://doi.org/10.1016/j.coal.2016.04.007.

Babaahmadi, A., Brooks, P. & Grant, M. (2021) Post-orogenic structural style and reactivation in the northern Bowen Basin, eastern Australia. *Australian Journal of Earth Sciences*, *68*(2), 188–203. https://doi.org/10.1080/08120099.2020.1767206.

Babaahmadi, A., Sliwa, R., Esterle, J. & Rosenbaum, G. (2017) The development of a Triassic fold-thrust belt in a synclinal depositional system, Bowen Basin (eastern Australia). *Tectonics*, *36*(1), 51–77. https://doi.org/10.1002/2016TC004297.

Baker, J.C. (1997) Green ferric clay in non-marine sandstones of the Rewan Group, southern Bowen Basin, eastern Australia. *Clay Minerals*, *32*(4), 499–506.

Bashari, A. (2000) Petrography and clay mineralogy of volcanoclastic sandstones in the Triassic Rewan Group, Bowen Basin, Australia. *Petroleum Geoscience*, *6*(2), 151–163. https://doi.org/10.1144/petgeo.6.2.151.

Brakel, A.T., Totterdell, J.M., Wells, A.T. & Nicoll, M.G. (2009) Sequence stratigraphy and fill history of the Bowen Basin, Queensland. *Australian Journal of Earth Sciences*, *56*(3), 401–432. https://doi.org/10.1080/08120090802698711.

Campbell, M.J., Hoy, D., Rosenbaum, G., Fielding, C. & Allen, C.M. (2022) The Onset of Gondwanide Orogeny in Eastern Australia: Insight From the Provenance of Syn-Orogenic Strata in the New England Orogen (Australia). *Tectonics*, *41*(2). https://doi.org/10.1029/2021TC006940.

Campbell, M.J., Shaanan, U. & Verdel, C. (2017) Fold-interference patterns in the Bowen Basin, northeastern Australia. *Australian Journal of Earth Sciences*, *64*(5), 577–585. https://doi.org/10.1080/08120099.2017.1334704.

Carraro, D., Gaynor, S.P., Ventra, D., Ulyanov, A. & Moscariello, A. (2024) Testing the fidelity of zircon as a provenance indicator in fluvial-fan successions: An example from the Palaeogene Colton Formation, Central Utah, USA. *Depositional Record*. https://doi.org/10.1002/dep2.316.

Castelltort, S., Fillon, C., Lasseur, É., Ortiz, A., Robin, C., Guillocheau, F., Tremblin, M., Bessin, P., Guerit, L., Dekoninck, A., Allanic, C., Gautheron, C., Barbarand, J., Loget, N., Uzel, J., Yans, J., Briais, J., Al-Reda, M., Baby, G., François, T., Roig, J.-Y. & Calassou, S. (2023) The Source-to-Sink Vade-mecum: History, Concepts and Tools | Vade-mecum de l'approche Source-To-Sink: Histoire, Concepts et Outils. *The Source-to-Sink Vade-Mecum: History, Concepts and Tools | Vade-Mecum de l'approche Source-To-Sink: Histoire, Concepts et Outils*. https://doi.org/10.2110/SEPMCSP.16.

Cawood, P.A., Hawkesworth, C.J. & Dhuime, B. (2012) Detrital zircon record and tectonic setting. *Geology*, *40*(10), 875–878. https://doi.org/10.1130/G32945.1.

Collins, W.J. (1991) A reassessment of the 'Hunter-Bowen Orogeny': Tectonic implications for the southern New England Fold Belt. *Australian Journal of Earth Sciences*, *38*(4), 409–423. https://doi.org/10.1080/08120099108727981.

Coutts, D.S., Matthews, W.A. & Hubbard, S.M. (2019) Assessment of widely used methods to derive depositional ages from detrital zircon populations. *Geoscience Frontiers*, *10*(4), 1421–1435. https://doi.org/10.1016/j.gsf.2018.11.002.

Danis, C., O'Neill, C. & Lackie, M. (2012) Building 3D geological knowledge through regional scale gravity modelling for the Bowen Basin. *Exploration Geophysics*. pp. 8–25. https://doi.org/10.1071/EG11028.

DeCelles, P.G. & Burden, E.T. (1992) Non-marine sedimentation in the overfilled part of the jurassic-cretaceous Cordilleran foreland basin: Morrison and Cloverly Formations, central Wyoming, USA. *Basin Research*, *4*(3–4), 291–314. https://doi.org/10.1111/j.1365-2117.1992.tb00050.x.

DeGraaff-Surpless, K., Mahoney, J.B., Wooden, J.L. & McWilliams, M.O. (2003) Lithofacies control in detrital zircon provenance studies: Insights from the Cretaceous Methow basin, southern Canadian Cordillera. *Geological Society of America Bulletin*, *115*(8), 899–915. https://doi.org/10.1130/B25267.1.

Dickinson, W.R. & Gehrels, G.E. (2009) Use of U–Pb ages of detrital zircons to infer maximum depositional ages of strata: A test against a Colorado Plateau Mesozoic database. *Earth and Planetary Science Letters*, *288*(1–2), 115–125. https://doi.org/10.1016/J.EPSL.2009.09.013.

Dickinson, W.R. & Suczek, C. (1979) Plate Tectonics and Sandstone Compositions. *AAPG Bulletin*, *63*(12), 2164–2182. https://doi.org/10.1306/2F9188FB-16CE-11D7-8645000102C1865D.

Dutta, P.K. & Wheat, R.W. (1993) Climatic and tectonic control on sandstone composition in the Permo-Triassic Sydney foreland basin, eastern Australia. *Special Paper of the Geological Society of America*, *284*, 187–202. https://doi.org/10.1130/SPE284-p187.

Exon, N.F.. (1976) *Geology of the Surat Basin in Queensland*. Australian Government Pub. Service.

Fielding, C.R., Frank, T.D., Savatic, K., Mays, C., McLoughlin, S., Vajda, V. & Nicoll, R.S. (2022) Environmental change in the late Permian of Queensland, NE Australia: The warmup to the end-Permian Extinction. *Palaeogeography, Palaeoclimatology, Palaeoecology*, *594*. https://doi.org/10.1016/j.palaeo.2022.110936.

Fielding, C.R., Stephens, C.J. & Holcombe, R.J. (1997) *Permian stratigraphy and palaeogeography of the eastern Bowen Basin, Gogango Overfolded Zone and Strathmuir Synclinorium in the Rockhampton-Mackay region, central Queensland*.

Foley, E.K., Baty, M., Knutsen, E.M., Lignum, J.S. & Roberts, E.M. (2020) Jurassic - Early Cretaceous paleogeography and paleoenvironments of the north-eastern margin of Gondwana: Insights from the Carpentaria Basin, Australia. *Gondwana Research*, *88*, 126–149. https://doi.org/10.1016/j.gr.2020.07.003.

Foley, E.K., Henderson, R.A., Roberts, E.M., Kemp, A.I.S., Todd, C.N., Knutsen, E.M., Fisher, C., Wainman, C.C. & Spandler, C. (2021) Jurassic Arc: Reconstructing the Lost World of eastern Gondwana. *Geology*, *49*(11), 1391–1396. https://doi.org/10.1130/G49328.1.

Garzanti, E. (2016) From static to dynamic provenance analysis—Sedimentary petrology upgraded. *Sedimentary Geology*, *336*, 3–13. https://doi.org/10.1016/J.SEDGEO.2015.07.010.

Garzanti, E. (2019) Petrographic classification of sand and sandstone. *Earth-Science Reviews*. Elsevier B.V., pp. 545–563. https://doi.org/10.1016/j.earscirev.2018.12.014.

Glen, R.A. (2005) The Tasmanides of eastern Australia. *Geological Society Special Publication*. pp. 23–96. https://doi.org/10.1144/GSL.SP.2005.246.01.02.

Gómez, R., Lothari, L., Tunik, M. & Casadio, S. (2019) Onset of foreland basin deposition in the Neuquén Basin (34°-35°S): New data from sedimentary petrology and U–Pb dating of detrital zircons from the Upper Cretaceous non-marine deposits. *Journal of South American Earth Sciences*, *95*(2), 102257. https://doi.org/10.1016/j.jsames.2019.102257.

Grech, P. V (2001) *Sedimentology and sequence stratigraphy of the Early Triassic Rewan Group, Bowen Basin* (Doctoral dissertation). The University of Adelaide.

Green, P.M., Carmichael, D.C., Brain, T.J., Murray, C.G., McKellar, J., Beeston, J.W. & Gray, A.R.G. (1997) Lithostratigraphic units in the Bowen and Surat Basins, Queensland. *The Surat and Bowen Basins, South-East Queensland*, 41–108.

Henderson, R.A. & Fergusson, C.L. (2019) Growth and provenance of a Paleozoic subduction complex in the Broken River Province, Mossman Orogen: evidence from detrital zircon ages. *Australian Journal of Earth Sciences*, *66*(5), 607–624. https://doi.org/10.1080/08120099.2019.1572033.

Hoy, D. (2020) *The Hunter-Bowen Orogeny in eastern Australia*.

Hoy, D., Rosenbaum, G., Mortimer, N. & Shaanan, U. (2018) Hunter–Bowen deformation in South Percy Island, northeastern Australia. *Australian Journal of Earth Sciences*, *65*(2), 175–190. https://doi.org/10.1080/08120099.2018.1419506.

Ingersoll, R., Bullard, T., Ford, R.L., Grimm, J.P., Pickle, J.D. & Sares, S.W. (1984) The effect of grain size on detrital modes: a test of the Gazzi- Dickinson point-counting method (Holocene, sand, New Mexico, USA). *Journal of Sedimentary Petrology*, *54*, 103–116.

Jell, P.A. (2013) *Geology of Queensland*. Geological Survey of Queensland.

Jensen, A.R. (1975) *Permo-Triassic stratigraphy and sedimentation in the Bowen Basin, Queensland*. Canberra.

Jessop, K., Daczko, N.R. & Piazolo, S. (2019) Tectonic cycles of the New England Orogen, eastern Australia: A Review. *Australian Journal of Earth Sciences*. Taylor and Francis Ltd., pp. 459–496. https://doi.org/10.1080/08120099.2018.1548378.

Kassan, J. (1994) *Basin analysis of the Triassic succession, Bowen Basin, Queensland*. The University of Queensland. https://doi.org/10.14264/293525.

Korsch, R.J., Totterdell, J.M., Cathro, D.L. & Nicoll, M.G. (2009) Early Permian East Australian Rift System. *Australian Journal of Earth Sciences*, *56*(3), 381–400. https://doi.org/10.1080/08120090802698703.

Korsch, R.J., Totterdell, J.M., Fomin, T. & Nicoll, M.G. (2009) Contractional structures and deformational events in the Bowen, Gunnedah and Surat Basins, eastern Australia. *Australian Journal of Earth Sciences*, *56*(3), 477–499. https://doi.org/10.1080/08120090802698745.

Lang, S.C., Grech, P., Root, R., Hill, A. & Harrison, D. (2001) THE APPLICATION OF SEQUENCE STRATIGRAPHY TO EXPLORATION AND RESERVOIR DEVELOPMENT IN THE COOPER-EROMANGA-BOWEN-SURAT BASIN SYSTEM. *The APPEA Journal*, *41*(1), 223. https://doi.org/10.1071/aj00011.

Li, P., Rosenbaum, G. & Donchak, P.J.T. (2012) Structural evolution of the Texas Orocline, eastern Australia. *Gondwana Research*, *22*(1), 279–289. https://doi.org/10.1016/j.gr.2011.09.009.

Li, P., Rosenbaum, G., Yang, J.H. & Hoy, D. (2015) Australian-derived detrital zircons in the Permian-Triassic Gympie terrane (eastern Australia): Evidence for an autochthonous origin. *Tectonics*, *34*(5), 858–874. https://doi.org/10.1002/2015TC003829.

Li, P.F., Rosenbaum, G. & Rubatto, D. (2012) Triassic asymmetric subduction rollback in the southern New England Orogen (eastern Australia): the end of the Hunter-Bowen Orogeny. *Australian Journal of Earth Sciences*, *59*(6), 965–981. https://doi.org/10.1080/08120099.2012.696556.

Lipp, A. & Vermeesch, P. (2022) Short communication: The Wasserstein distance as a dissimilarity metric for comparing detrital age spectra and other geological distributions. *Geochronology*, *5*(1), 263–270. https://doi.org/10.5194/gchron-5-263-2023.

Maravelis, A.G., Offler, R., Botziolis, C., Pantopoulos, G., Scott, A., Landenberger, B. & Collins, W.J. (2023) Provenance of a Late Permian retroarc foreland basin along the eastern Gondwanan margin: northern Sydney Basin, eastern Australia. *Geological Magazine*, *160*(8), 1535–1555. https://doi.org/10.1017/S0016756823000535.

Mason, C.C., Romans, B.W., Patterson, M.O., Stockli, D.F. & Fildani, A. (2022) Cycles of Andean mountain building archived in the Amazon Fan. *Nature Communications 2022 13:1*, *13*(1), 6983-. https://doi.org/10.1038/s41467-022-34561-6.

McKellar, J.L., Ayaz, A., Laurie Geoscience Australia, J.R., Nicoll, R., McKellar, J., Areeba Ayaz, S., Laurie, J., Esterle, J., Crowley, J., Wood, G. & Bodorkos, S. (2015) *CA-IDTIMS dating of tuffs, calibration of palynostratigraphy and stratigraphy of the Bowen and Galilee basins*.

Michaelsen, P. & Henderson, R.A. (2000) Sandstone petrofacies expressions of multiphase basinal tectonics and arc magmatism: Permian-Triassic north Bowen Basin, Australia. *Sedimentary Geology*, *136*(1–2), 113–136. https://doi.org/10.1016/S0037-0738(00)00090-7.

Naher, J., Fielding, C.R. & Martin, M.A. (2025) Misleading Basin Margins—Analysis of the Upper Permian Succession in the Retroarc Foreland Bowen Basin of Northeast Australia. *Basin Research*, *37*(3), e70033. https://doi.org/10.1111/BRE.70033.

Paton, C., Hellstrom, J., Paul, B., Woodhead, J. & Hergt, J. (2011) Iolite: Freeware for the visualisation and processing of mass spectrometric data. *Journal of Analytical Atomic Spectrometry*, *26*(12), 2508–2518. https://doi.org/10.1039/C1JA10172B.

Phillips, G., Landenberger, B. & Belousova, E.A. (2011) Building the New England Batholith, eastern Australia—Linking granite petrogenesis with geodynamic setting using Hf isotopes in zircon. *Lithos*, *122*(1–2), 1–12. https://doi.org/10.1016/J.LITHOS.2010.11.005.

Phillips, L.J., Edwards, S.A., Bianchi, V. & Esterle, J.S. (2017) Paleo-environmental reconstruction of Lopingian (upper Permian) sediments in the Galilee Basin, Queensland, Australia. *Australian Journal of Earth Sciences*, *64*(5), 587–609. https://doi.org/10.1080/08120099.2017.1338618.

Phillips, L.J., Verdel, C., Allen, C.M. & Esterle, J.S. (2018) Detrital zircon U–Pb geochronology of Permian strata in the Galilee Basin, Queensland, Australia. *Australian Journal of Earth Sciences*, *65*(4), 465–481. https://doi.org/10.1080/08120099.2018.1467261.

Purdy, D.J., Cross, A.J., Brown, D.D., Carr, P.A. & Armstrong, R.A. (2016) New constraints on the origin and evolution of the Thomson Orogen and links with central Australia from isotopic studies of detrital zircons. *Gondwana Research*, *39*, 41–56. https://doi.org/10.1016/J.GR.2016.06.010.

Romans, B.W., Castelltort, S., Covault, J.A., Fildani, A. & Walsh, J.P. (2016) Environmental signal propagation in sedimentary systems across timescales. *Earth-Science Reviews*, *153*(6), 7–29. https://doi.org/10.1016/j.earscirev.2015.07.012.

Rosenbaum, G. (2026) The plate tectonic setting of mineral deposits in the New England Orogen (Australia). *Earth-Science Reviews*, *276*, 105435. https://doi.org/10.1016/j.earscirev.2026.105435.

Rosenbaum, G., Babaahmadi, A., Glorie, S. & Schellart, W.P. (2025) Development of arc curvature by asymmetric migration: Evidence from Permian–Triassic granitoids in the New England Orogen (eastern Australia). *Earth and Planetary Science Letters*, *653*, 119209. https://doi.org/10.1016/J.EPSL.2025.119209.

Rosenbaum, G., Slade, A. & Hoy, D. (2020) Sedimentological responses to the Hunter–Bowen Orogeny (eastern Australia): evidence from the northern Gympie Terrane. *Australian Journal of Earth Sciences*, *67*(1), 59–73. https://doi.org/10.1080/08120099.2019.1648317.

Scipione, M., Vaucher, R., Roberts, E., McCoy-West, A.J., Esterle, J., Turner, A. & Knutsen, E. (2026) Shifting the Paradigm: Redefining the Chronostratigraphy of the Triassic Rewan Group, Bowen Basin, Australia. *Basin Research*, *38*(3), e70102. https://doi.org/10.1111/BRE.70102.

Shaanan, U. & Rosenbaum, G. (2018) Detrital zircons as palaeodrainage indicators: insights into southeastern Gondwana from Permian basins in eastern Australia. *Basin Research*, *30*, 36–47. https://doi.org/10.1111/bre.12204.

Shaanan, U., Rosenbaum, G. & Sihombing, F.M.H. (2018) Continuation of the Ross–Delamerian Orogen: insights from eastern Australian detrital-zircon data. *Australian Journal of Earth Sciences*, *65*(7–8), 1123–1131. https://doi.org/10.1080/08120099.2017.1354916.

Shaw, S.E., Flood, R.H. & Pearson, N.J. (2011) The New England Batholith of eastern Australia: Evidence of silicic magma mixing from zircon 176Hf/177Hf ratios. *Lithos*, *126*(1–2), 115–126. https://doi.org/10.1016/J.LITHOS.2011.06.011.

Siegel, C., Bryan, S.E., Allen, C.M., Gust, D.A. & Purdy, D.J. (2020) Crustal evolution in the New England orogen, Australia: Repeated igneous activity and scale of magmatism govern the composition and isotopic character of the continental crust. *Journal of Petrology*, *61*(8). https://doi.org/10.1093/petrology/egaa078.

Sliwa, R., Babaahmadi, A. & Esterle, J. (2018) *ACARP Project C24032: Structure Supermodel 2017-Fault Characterisation in Permian to Jurassic Coal Measures For the Australian Coal Association Research Program (ACARP)*.

Sobczak, K., La Croix, A.D., Esterle, J., Hayes, P., Holl, H.G., Ciesiolka, R., Crowley, J.L. & Allen, C.M. (2022) Geochronology and sediment provenance of the Precipice Sandstone and Evergreen Formation in the Surat Basin, Australia: Implications for the palaeogeography of eastern Gondwana. *Gondwana Research*, *111*, 189–208. https://doi.org/10.1016/j.gr.2022.08.003.

Spampinato, G.P.T., Betts, P.G., Ailleres, L. & Armit, R.J. (2015) Early tectonic evolution of the Thomson Orogen in Queensland inferred from constrained magnetic and gravity data. *Tectonophysics*, *651–652*, 99–120. https://doi.org/10.1016/J.TECTO.2015.03.016.

Sylvester, P.J., Souders, A.K. & Liu, R. (2022) Significance of U-Pb detrital zircon geochronology for mudstone provenance. *Geology*, *50*(6), 670–675. https://doi.org/10.1130/G49684.1.

Todd, C. (2020) The sedimentary evolution of Permian to Cretaceous basins in Queensland, Australia: insights from lithostratigraphy, U–Pb zircon geochronology, sedimentary facies, and provenance analysis. https://doi.org/10.25903/x1pq%2Dxc37.

Todd, C.N., Roberts, E.M. & Charles, A.J. (2022) A revised Permian–Triassic stratigraphic framework for the northeastern Galilee Basin, Queensland, Australia, and definition of a new Middle–Upper Triassic sedimentary unit. *Australian Journal of Earth Sciences*, *69*(1), 113–134. https://doi.org/10.1080/08120099.2021.1931962.

Tucker, R.T., Roberts, E.M., Henderson, R.A. & Kemp, A.I.S. (2016) Large igneous province or long-lived magmatic arc along the eastern margin of Australia during the Cretaceous? Insights from the sedimentary record. *Bulletin of the Geological Society of America*, *128*(9–10), 1461–1480. https://doi.org/10.1130/B31337.1.

Tucker, R.T., Roberts, E.M., Hu, Y., Kemp, A.I.S. & Salisbury, S.W. (2013) Detrital zircon age constraints for the Winton Formation, Queensland: Contextualizing Australia's Late Cretaceous dinosaur faunas. *Gondwana Research*, *24*(2), 767–779. https://doi.org/10.1016/J.GR.2012.12.009.

Van Heeswijck, A. (2010) Late paleozoic to early Mesozoic deformation in the northeastern Galilee Basin, Australia. *Australian Journal of Earth Sciences*, *57*(4), 431–451. https://doi.org/10.1080/08120099.2010.481328.

Van Heeswijck, A. (2018) Fluvial sequences and basin development in the northern Galilee Basin. *Australian Journal of Earth Sciences*, *65*(3), 367–389. https://doi.org/10.1080/08120099.2018.1437772.

Vermeesch, P. (2012) On the visualisation of detrital age distributions. *Chemical Geology*, *312–313*, 190–194. https://doi.org/10.1016/J.CHEMGEO.2012.04.021.

Vermeesch, P. (2018) IsoplotR: A free and open toolbox for geochronology. *Geoscience Frontiers*, *9*(5), 1479–1493. https://doi.org/10.1016/J.GSF.2018.04.001.

Vermeesch, P. (2021) Maximum depositional age estimation revisited. *Geoscience Frontiers*, *12*(2), 843–850. https://doi.org/10.1016/J.GSF.2020.08.008.